JGR Solid Earth

RESEARCH ARTICLE
10.1029/2018JB016598

High-Resolution Constraints on Pacific Upper Mantle Petrofabric Inferred From Surface-Wave Anisotropy

Joshua B. Russell[1], James B. Gaherty[1], Pei-Ying Patty Lin[2], Daniel Lizarralde[3], John A. Collins[3], Greg Hirth[4], and Rob L. Evans[3]

[1]Lamont-Doherty Earth Observatory, Columbia University, Palisades, NY, USA, [2]Department of Earth Sciences, National Taiwan Normal University, Taipei, Taiwan, [3]Department of Geology and Geophysics, Woods Hole Oceanographic Institution, Falmouth, MA, USA, [4]Geological Sciences Department, Brown University, Providence, RI, USA

Key Points:
- In situ seismic anisotropy in oceanic mantle lithosphere agrees with ophiolite petrofabrics, linking outcrop and surface-wave length scales
- Lithospheric mantle anisotropy is consistent with flow model predictions of fabric produced by passive upwelling at the mid-ocean ridge
- Strong radial anisotropy in the lower crust suggests horizontal layering and/or shearing during crustal accretion

Supporting Information:
- Supporting Information S1
- Data Set S1

Correspondence to:
J. B. Russell,
jrussell@ldeo.columbia.edu

Citation:
Russell, J. B., Gaherty, J. B., Lin, P.-Y. P., Lizarralde, D., Collins, J. A., Hirth, G., & Evans, R. L. (2019). High-resolution constraints on Pacific upper mantle petrofabric inferred from surface-wave anisotropy. *Journal of Geophysical Research: Solid Earth*, *124*, 631–657. https://doi.org/10.1029/2018JB016598

Received 28 AUG 2018
Accepted 21 DEC 2018
Accepted article online 26 DEC 2018
Published online 17 JAN 2019

Abstract Lithospheric seismic anisotropy illuminates mid-ocean ridge dynamics and the thermal evolution of oceanic plates. We utilize short-period (5–7.5 s) ambient-noise surface waves and 15- to 150-s Rayleigh waves measured across the NoMelt ocean-bottom array to invert for the complete radial and azimuthal anisotropy in the upper ~35 km of ~70-Ma Pacific lithospheric mantle, and azimuthal anisotropy through the underlying asthenosphere. Strong azimuthal variations in Rayleigh- and Love-wave velocity are observed, including the first clearly measured Love-wave 2θ and 4θ variations. Inversion of averaged dispersion requires radial anisotropy in the shallow mantle (2-3%) and the lower crust (4-5%), with horizontal velocities (V_{SH}) faster than vertical velocities (V_{SV}). Azimuthal anisotropy is strong in the mantle, with 4.5–6% 2θ variation in V_{SV} with fast propagation parallel to the fossil-spreading direction (FSD), and 2–2.5% 4θ variation in V_{SH} with a fast direction 45° from FSD. The relative behavior of 2θ, 4θ, and radial anisotropy in the mantle are consistent with ophiolite petrofabrics, linking outcrop and surface-wave length scales. V_{SV} remains fast parallel to FSD to ~80 km depth where the direction changes, suggesting spreading-dominated deformation at the ridge. The transition at ~80 km perhaps marks the dehydration boundary and base of the lithosphere. Azimuthal anisotropy strength increases from the Moho to ~30 km depth, consistent with flow models of passive upwelling at the ridge. Strong azimuthal anisotropy suggests extremely coherent olivine fabric. Weaker radial anisotropy implies slightly nonhorizontal fabric or the presence of alternative (so-called E-type) peridotite fabric. Presence of radial anisotropy in the crust suggests subhorizontal layering and/or shearing during crustal accretion.

1. Introduction

Seafloor spreading at mid-ocean ridges (MORs) offers perhaps the most direct observational window into deformation associated with convection in the Earth's mantle. Solid-state shear deformation from the upward-and-outward trajectory of corner flow induces strong fabric in olivine-rich mantle rocks that can be readily observed at the hand and outcrop scale in ophiolites (e.g., Ismail & Mainprice, 1998; Nicolas & Christensen, 1987; Peselnick & Nicolas, 1978) and indirectly inferred from measurements of azimuthal seismic anisotropy in oceanic lithosphere at scales ranging from a ridge segment to an entire plate (e.g., Forsyth, 1975; Hess, 1964; Morris et al., 1969; Raitt et al., 1969). In particular, the [100] (*a*-) axes of olivine crystals, and the faster seismic wave speeds, both tend to align with the paleo-spreading direction in the shallow mantle lithosphere. The strong correspondence between this character of seismic anisotropy observed in ophiolites and seismic observations from oceanic lithosphere and that predicted in laboratory studies of simple shear in olivine (e.g., Karato et al., 2008; Zhang & Karato, 1995) and reproduced in modeling of polycrystalline materials (e.g., Kaminski & Ribe, 2001, 2002; Ribe, 1989) provides strong confidence that seismic anisotropy can be used to infer shear deformation and thus mantle flow. This correspondence is one of the key observations that underpins the widely applied practice of using seismic anisotropy to map flow direction in the upper mantle (e.g., see; Long & Silver, 2009; Savage, 1999, for reviews).

In detail, observations suggest significant complexity in the apparent relationship between deformation processes and seismic anisotropy. Early refraction experiments in the Pacific recorded slight misalignment between the fast propagation direction of P_n and paleo-spreading direction (e.g., Keen & Barrett,

1971; Morris et al., 1969). These early findings are corroborated by a growing body of seismic observations from the oceanic lithosphere documenting variations in anisotropic fabric that appear to depend on seafloor-spreading rate (e.g., Gaherty et al., 2004), differences in relative versus absolute plate motion (APM) at the ridge (e.g., Toomey et al., 2007; Takeo et al., 2016; Vanderbeek & Toomey, 2017), and/or the nature of upwelling beneath the ridge (e.g., Delorey et al., 2007; Gaherty, 2001). In the oldest reaches of the Pacific, the lithospheric anisotropy varies over relatively short length scales and does not always correlate with the direction of seafloor spreading (e.g., Shintaku et al., 2014; Takeo et al., 2016, 2018). These observations suggest a rich diversity of dynamic processes beneath MORs that go well beyond the simple symmetrical-spreading models explored to date (e.g., Blackman et al., 1996; Blackman & Kendall, 2002a; Blackman et al., 2017).

Observations of seismic anisotropy produced by a given fabric take different forms depending on the type of seismic data being analyzed. The alignment of olivine's fast [100] axis parallel to spreading should produce measurable wave speed perturbations to horizontally propagating seismic waves depending on (1) the propagation direction of the wave relative to the olivine [100] axis (azimuthal anisotropy) and (2) the shear-wave polarization angle relative to the fabric plane (radial anisotropy). In the ocean basins, the former is generally measured on P and S waves traveling subhorizontally in the shallow mantle, and on Rayleigh waves from earthquakes and ambient noise. The latter is observed as a discrepancy between the azimuthally averaged velocity of Rayleigh and Love waves relative to an isotropic model, which can be modeled as the difference in shear velocities (V_{SV} and V_{SH}) experienced by horizontally propagating, vertically and horizontally polarized shear waves, respectively (e.g., Anderson & Dziewonski, 1982). For a given underlying olivine fabric, the two types of anisotropy can be related to one another in a predictable way and should be consistent. However, most observations of anisotropy only quantify a small subset of the possible anisotropic parameters, and little attention is generally paid to whether anisotropy models derived from different subsets of data sampling the same region are consistent with a common peridotite fabric. As a result, the observations are used to qualitatively assess MOR models, rather than provide quantitative constraints on deformation and flow.

In this study, we provide the first high-resolution constraints on a complete parameterization of shear-wave anisotropy (including Love waves) in the oceanic lithosphere. We utilize short-period (5–7.5 s) ambient-noise surface-wave observations in conjunction with previously measured 15–150 s Rayleigh waves (Lin et al., 2016) recorded on an array of ocean-bottom seismometers (OBS) deployed on 70-Ma seafloor in the central Pacific. Strong azimuthal and radial anisotropy are observed in both Rayleigh- and Love-wave phase velocities, including perhaps the first clearly observed 2θ and 4θ variations in Love-wave velocities. Although radial and azimuthal anisotropy have been previously observed in the Pacific, this study is one of the first to explicitly solve for and interpret together both types of anisotropy within a relatively small footprint. The resulting shear-anisotropy model is compared to observed petrofabrics from oceanic environments and discussed in the context of improving models of MOR dynamics.

2. A Comprehensive Model of Seismic Anisotropy

The lattice-preferred orientation (LPO) of olivine produces observable seismic body- and surface-wave anisotropy that can be used to infer past and present deformation patterns in the mantle (Mainprice, 2015). For weak anisotropy appropriate for olivine, 13 elastic parameters are required to fully model anisotropy observed in surface waves (see Appendix A). In practice, these parameters are often separated into the azimuthally averaged components that control radial anisotropy and those that control the azimuthal variations relative to these averages. Our analysis incorporates the full set of 13 parameters, as defined by Montagner and Nataf (1986) and fully described in Appendix A. Here we summarize the dominant shear-velocity components that are the focus of our analysis.

To first order, Rayleigh waves are sensitive to the horizontally propagating vertically polarized shear wave speed V_{SV} (or the parameter L), and Love waves are dominantly sensitive to V_{SH} (or the parameter N). Radial anisotropy ($\xi = V_{SH}^2/V_{SV}^2$) is constrained by azimuthally averaged Rayleigh- and Love-wave velocities and is a proxy for the degree that the underlying fabric is organized with fast axes that are predominantly subhorizontal ($\xi > 1$) or subvertical ($\xi < 1$) (e.g., Anderson & Dziewonski, 1982). If the LPO fabric is organized laterally over seismic length scales, then azimuthal anisotropy also occurs, where V_{SV} displays a 2θ variability described by a peak-to-peak amplitude (parameter G) and fast direction of propagation (Ψ_G). Similarly, V_{SH} displays a 4θ azimuthal variability controlled by parameters E and Ψ_E. Anisotropic fabric of

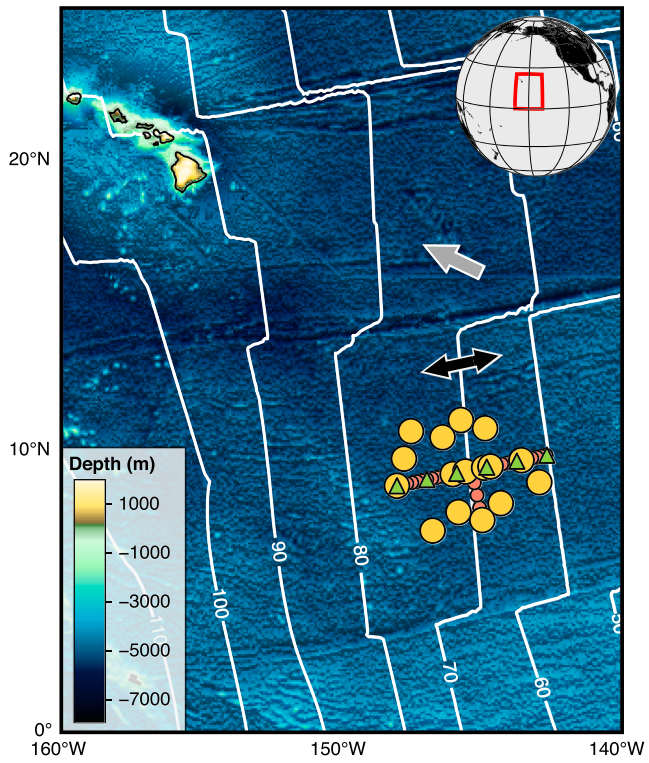

Figure 1. The 600 × 400 km NoMelt array consisting of 16 broadband ocean-bottom seismometers (yellow large circles), 34 short-period ocean-bottom seismometers (red smaller circles), and 6 magnetotelluric instruments (green triangles; Sarafian et al., 2015). White solid lines show ocean floor isochrons in increments of 10 Ma (Müller et al., 2008). The gray arrow shows the absolute plate motion direction (Argus & Gordon, 1991), and the black double-headed arrow shows the fossil-spreading direction in the NoMelt region.

this form results in Rayleigh waves with a 2θ azimuthal variability and Love waves with both a 2θ and 4θ variability (Montagner & Nataf, 1986).

In this study, we model the full azimuthal variability of Rayleigh- and Love-wave velocities to constrain radial (ξ) and azimuthal anisotropy (G, Ψ_G, E, Ψ_E) at NoMelt (Figure 1), including the first observations of 2θ and 4θ Love-wave anisotropy and E in the lithosphere. We utilize additional scaling relations derived from oceanic peridotites from the literature as well as scaling between P and S wave speeds to solve for the remaining seven elastic parameters, resulting in the first local-scale estimate of the complete in situ anisotropic fabric of oceanic lithosphere.

3. Anisotropy of the Pacific and the NoMelt Experiment

The Pacific is especially well-suited for investigating plate evolution and MOR processes due to its broad range of plate ages, excellent distribution of seismic sources, and the recent proliferation of onshore and offshore data. Radial and azimuthal anisotropy have been extensively studied in the Pacific upper mantle at regional (Forsyth, 1975; Forsyth et al., 1998; French & Romanowicz, 2014; Gaherty et al., 1996; Lin et al., 2016; Nishimura & Forsyth, 1989; Tan & Helmberger, 2007; Takeo et al., 2013, 2014, 2016, 2018; Weeraratne et al., 2007) and global scales (Beghein et al., 2014; Debayle & Ricard, 2013; Ekström & Dziewonski, 1998; Montagner & Tanimoto, 1990, 1991; Moulik & Ekström, 2014; Montagner, 2002; Nettles & Dziewoński, 2008; Schaeffer et al., 2016; Yuan & Beghein, 2013), providing a comprehensive picture of the upper mantle LPO and flow field.

Surface-wave observations of azimuthal anisotropy predominantly show fast propagation directions approximately parallel to the fossil-spreading direction (FSD) in the lithosphere (Beghein et al., 2014; Forsyth, 1975; Lin et al., 2016; Montagner, 2002; Schaeffer et al., 2016; Takeo et al., 2014) and approximately parallel to APM direction in the asthenosphere (Beghein et al., 2014; Nishimura & Forsyth, 1989; Schaeffer et al., 2016; Takeo et al., 2016). Furthermore, mantle-refracted P_n waves propagate through the uppermost lithosphere with a fast direction parallel to the FSD (Hess, 1964; Raitt et al., 1969). This FSD parallel anisotropy in the lithosphere suggests quasi-horizontal alignment of olivine [100] crystallographic axes and is consistent with strain localization due to corner flow at the MOR during plate formation (Blackman & Kendall, 2002a).

The strength of azimuthal anisotropy in the lithosphere is less well constrained, however, appearing weaker than the asthenosphere in some models (Beghein et al., 2014; Schaeffer et al., 2016; Yuan & Beghein, 2013) and stronger in others (Lin et al., 2016; Nishimura & Forsyth, 1989; Rychert & Harmon, 2017; Takeo et al., 2016, 2018). Observations of radial anisotropy in the low velocity zone (LVZ) beneath the Pacific plate show $\xi > 1$, suggesting horizontal fabric interpreted as low-viscosity channels of flow (Beghein et al., 2014; Nettles & Dziewoński, 2008). However, the strength and even the sign of lithospheric radial anisotropy vary widely between models (see section 7.2). The lack of agreement between models of lithosphere anisotropy (both radial and azimuthal) can perhaps be attributed to poor shallow resolution and lateral smearing inherent in plate-scale models, thus emphasizing the need for new high-resolution, local-scale measurements.

The NoMelt array, situated on 70-Ma lithosphere, was designed to provide high-resolution surface-wave constraints over a relatively undeformed region in the Pacific basin in order to better understand the first-order lithosphere-asthenosphere structure (Figure 1). Previously, Lin et al. (2016) utilized Rayleigh waves from teleseismic earthquakes (20–150 s) and ambient noise (10–20 s) to characterize V_{SV} and azimuthal anisotropy (G) down to ~300 km depth beneath NoMelt. In the lithosphere, they observe Ψ_G parallel to the FSD (~ 78°), consistent with previous studies and with new active-source constraints on P wave anisotropy just beneath the Moho at NoMelt (Mark et al., 2017). However, the direction of anisotropy in the

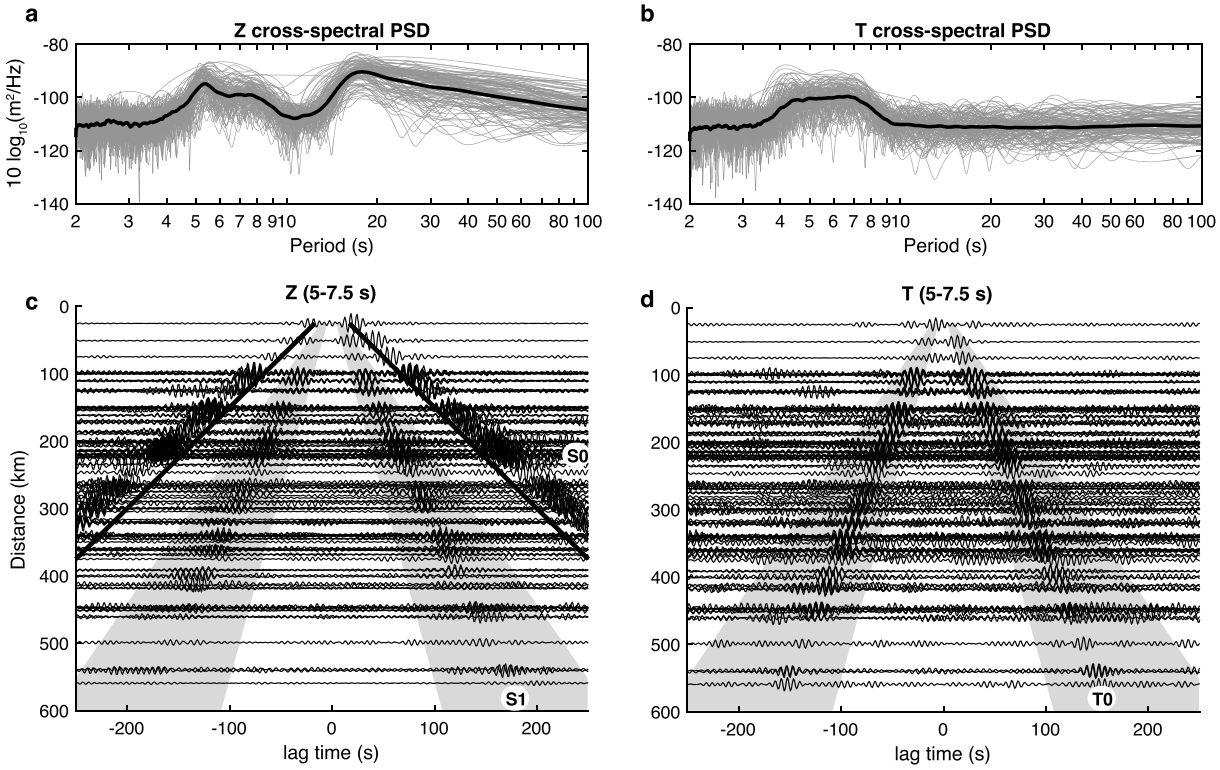

Figure 2. Cross-spectral power spectral density (PSD) and empirical Green's functions for Rayleigh and Love waves. (a) Average PSD calculated from the year-averaged cross-spectra for Rayleigh waves on the vertical component. The primary microseism peaks at 20 s, and the secondary microseism at 5–7.5 s. Station pair PSDs are shown by thin gray lines and their mean in black. (b) Same as (a) but for Love waves on the transverse component. Note that only the secondary microseism peak (5–7.5 s) appears for the transverse component. (c) Vertical component empirical Green's functions band-pass filtered at 5–7.5 s period with the 2.2- to 5.5-km/s group-velocity window shaded in gray. The fundamental mode Rayleigh wave (S0) travels through the water column at these frequencies (~1.5 km/s, black line) and arrives outside the chosen group-velocity window. The first overtone Rayleigh wave (S1) arrives within the window. (d) Same as (b) but for the transverse component showing the fundamental mode Love wave (T0).

asthenosphere was neither parallel to FSD nor APM, suggesting secondary local-scale deformation processes that overprint the simple plate motion signal observed in many global and plate-scale models.

Our study utilizes high-frequency (5–7.5 s) Rayleigh and Love waves to provide updated high-resolution constraints on G as well as new constraints on B, H, E, and ξ in the upper ~30 km of the mantle to produce a complete anisotropic model of the oceanic lithosphere beneath NoMelt. In particular, we focus on the lithospheric strengths and directions of G, E, and ξ, providing quantitative estimates that are consistent with peridotite samples and predictions of LPO fabric formed at ridges.

4. Data

4.1. High-Frequency Ambient-Noise Processing

Twelve months of continuous data were collected on 16 high signal-to-noise, three-component broadband OBS instruments from January to December 2012. We follow the data processing procedures outlined in Bensen et al. (2007). The data are downsampled to 1 Hz, and the daily mean and trends are removed. The horizontal H1 and H2 components are then rotated to the radial and transverse orientations for each station pair. OBS orientations and their 4σ uncertainties are determined using the DLOPy method (Doran & Laske, 2017) with earthquakes >M7.0 (Table S1 in the supporting information). To minimize the influence of earthquakes on the noise spectra, we use a one-bit normalization procedure where the amplitude of each point in the time series is normalized by its absolute value such that a point is either −1 if negative or +1 if positive. Finally, the daily spectra are whitened to enhance localization of signals in the time domain.

Cross-correlations between station pairs are calculated in the frequency domain for each day of data on all three components (vertical, radial, and transverse) to extract the coherent ambient noise wavefield.

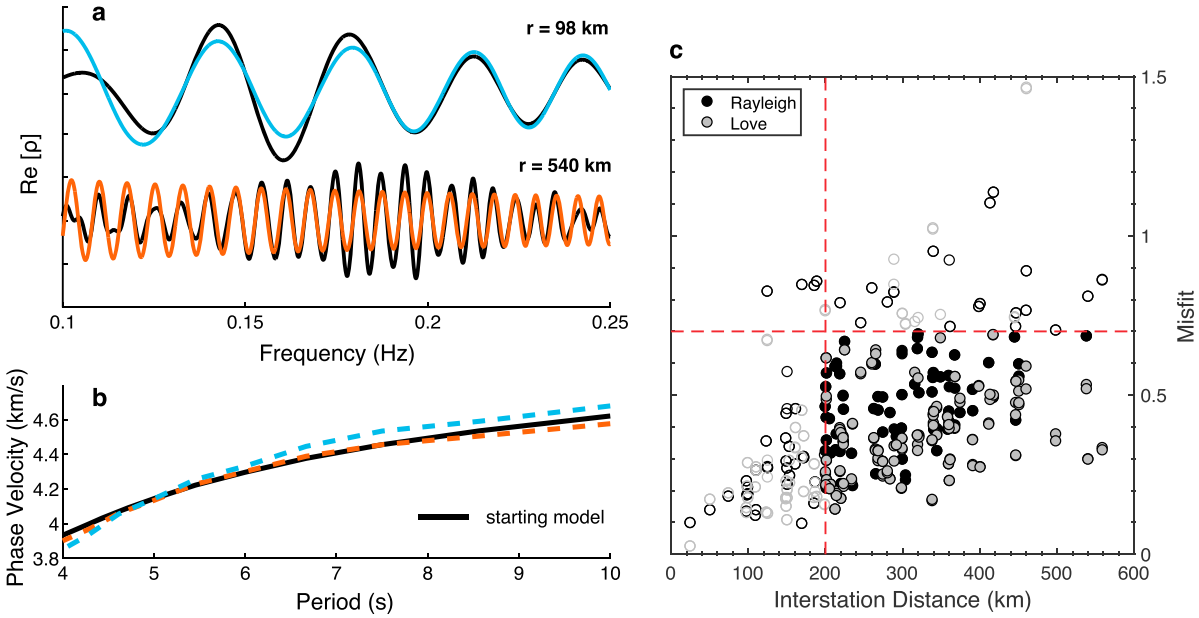

Figure 3. (a) An example of the Bessel function fitting procedure on the transverse component for extracting interstation Love-wave phase velocities. The real part of the cross-spectra, $\rho(\omega, r)$, for two stations separated by 98 and 540 km are plotted in black. The corresponding synthetic Bessel function fits using equation (1) are plotted in color. (b) Comparison of the starting phase velocity model, $c(\omega)$, in black and the final models dashed in color. Longer interstation distances have more zero crossings, thus providing a better constraint on phase velocity. (c) Misfit between the observed (ρ_{obs}) and predicted (ρ_{pre}) cross-spectra where misfit is defined as $\sum_\omega(\rho_{obs} - \rho_{pre})^2 / \sum_\omega \rho_{pre}^2$. To ensure the highest quality measurements, we use interstation distance and misfit cutoffs of 200 km and 0.7, respectively, shown by the red dashed lines. Open circles depict measurements that do not meet these standards.

Each station component is cross-correlated with the same component of a nearby station. To maximize signal-to-noise, each day of data is split into 15 three-hour segments with 50% overlap between neighboring segments. The 15 individual cross-spectra are then stacked together yielding a single daily cross-spectrum for each of the three components. These daily traces are then stacked over the entire year producing the final year-averaged cross-spectra.

The power spectral density and time-domain empirical Green's functions for the year-averaged cross-spectra are shown in Figure 2 for both vertical and transverse components. Rayleigh waves are recorded on the vertical component and Love waves on the transverse component. Comparing the cross-spectral power spectral densities of the two components (Figures 2a and 2b), we see a similar peak at 5- to 7.5-s period on both components, but the typical primary microseism peak at ~20 s is absent on the transverse component. In the time domain, the 5- to 7.5-s signal manifests itself as two distinct mode branches on the vertical component (Figure 2c). The slower traveling wave is the fundamental mode Rayleigh wave (S0) traveling through the water column at ~1.5 km/s, and the faster traveling wave is the first overtone Rayleigh wave (S1) traveling through the solid earth. On the transverse component, this frequency band contains only the fundamental mode Love wave (T0) traveling at a similar group velocity to the first overtone Rayleigh wave. In order to isolate the S1 and T0 mode branches and improve signal-to-noise, we apply a 2.2- to 5.5-km/s group-velocity cosine-tapered window to both the vertical and transverse components, shown by the gray shaded regions in Figures 2c and 2d.

4.2. Cross-Spectral Waveform Fitting

Phase velocities are measured from the windowed data using the cross-spectral formulation of Aki (1957). For a homogeneous noise source and interstation distances much longer than the wavelength of the waves being measured, the real parts of the vertical (Z) and transverse (T) cross-spectra, ρ, take the functional form (Aki, 1957; Cox, 1973)

$$\rho^{Z,T}(\omega, r) = A J_0\left(\frac{\omega r}{c^{R,L}(\omega)}\right), \quad (1)$$

where $c(\omega)$ is the interstation phase velocity of Rayleigh (R) or Love (L) waves at frequency ω, r is the interstation distance, J_0 is the Bessel function of order zero, and A is an amplitude prefactor. Equation (1) is only

valid for Love waves when r is much larger than the wavelength of the waves being measured, which is true for this study. Previous studies have included amplitude information, A, to extract dispersion from multiple mode branches (Nishida et al., 2008; Takeo et al., 2013, 2014, 2016, 2018). However, we have chosen to reduce the number of free parameters by letting $A = 1$, measuring dispersion for a single mode branch on each component, which is justified by our relatively tight group velocity window (Figure 2). Interstation phase velocities are extracted from 4- to 10-s period by fitting a Bessel function to the observed cross-spectra for each station pair (Figure 3) using the method of Menke and Jin (2015). Due to the decrease in signal at periods <5 and >7.5 s (Figures 2a and 2b) as well as possible Love-wave overtone interference at >7.5 s (Figure 5), this study utilizes the period range 5–7.5 s.

The fitting is performed on each station pair using a nonlinear least squares algorithm where the starting dispersion model is taken from Lin et al. (2016). The inversion is performed twice for each station pair. After the first inversion, the resulting dispersion curves for every station pair are weighted based on the misfit of each Bessel function and averaged together, yielding a single average dispersion curve. This average curve is then used as the starting model for the second iteration of the inversion. This procedure greatly reduces the degree of cycle skipping in the final Bessel function fits and is more convenient than performing a grid search to determine a suitable starting model. Examples of typical Bessel fits and their corresponding dispersion curves are shown in Figure 3 for long ($r = 540$ km) and short ($r = 98$ km) interstation distances. For short interstation distances, there are fewer zero crossings in the Bessel function, and therefore, the resulting dispersion curve is less well constrained. To ensure high-quality phase velocity measurements, only interstation distances ≥200 km are used in this study.

4.3. The 1-D Average Phase Velocities

We measure interstation phase-velocity dispersion of S1 and T0 mode branches for each station pair at 5–7.5 s, providing excellent azimuthal coverage within the array footprint. The collection of phase-velocity measurements are used to solve for the average (1-D) phase velocity, and an azimuthal variation relative to this average, for each wave type at each frequency. This 1-D approach is justified given the relatively small lateral variations in phase velocity (<1%) for both Rayleigh and Love waves at 5- to 7.5-s period (see Figures S1 and S2). In general, the azimuthal variability of phase velocity c, is given by (Montagner & Nataf, 1986)

$$\begin{aligned} c(\omega,\theta) =& c_0(\omega)\left[1 + A_{c2}(\omega)\cos(2\theta) + A_{s2}(\omega)\sin(2\theta)\right. \\ &\left. + A_{c4}(\omega)\cos(4\theta) + A_{s4}(\omega)\sin(4\theta)\right], \end{aligned} \tag{2}$$

where ω is the angular frequency of the wave, θ is the wave-propagation azimuth measured clockwise from north, and $A_i(\omega) = (\delta c/c)_i$ are the zero-to-peak amplitudes describing the azimuthal dependence of phase velocity. The term $c_0(\omega)$ is the isotropic phase velocity, which is independent of azimuth and captures radial anisotropy.

For Rayleigh waves, the 4θ terms A^R_{c4} and A^R_{s4} are nearly zero (Montagner & Nataf, 1986; see Figure S1) and therefore, the azimuthal dependence can be approximated as

$$c^R(\omega,\theta) = c^R_0(\omega)\left[1 + A^R_{c2}(\omega)\cos(2\theta) + A^R_{s2}(\omega)\sin(2\theta)\right], \tag{3}$$

or in terms of an amplitude A^R_2 and fast direction ψ^R_2:

$$c^R(\omega,\theta) = c^R_0\left[1 + A^R_2\cos 2\left(\theta - \psi^R_2\right)\right], \tag{4}$$

where $A^R_2 = \sqrt{(A^R_{c2})^2 + (A^R_{s2})^2}$ and $\psi^R_2 = 0.5\arctan\left(A^R_{s2}/A^R_{c2}\right)$. Love waves, on the other hand, require both 2θ and 4θ components to fully describe their azimuthal variation and therefore the equation for the azimuthal dependence of Love waves is given by

$$\begin{aligned} c^L(\omega,\theta) &= c^L_0(\omega)\left[1 + A^L_{c2}(\omega)\cos(2\theta) + A^L_{s2}(\omega)\sin(2\theta)\right. \\ &\quad \left. + A^L_{c4}(\omega)\cos(4\theta) + A^L_{s4}(\omega)\sin(4\theta)\right] \\ &= c^L_0\left[1 + A^L_2\cos 2\left(\theta - \psi^L_2\right) + A^L_4\cos 4\left(\theta - \psi^L_4\right)\right]. \end{aligned} \tag{5}$$

Sinusoidal functions are fit to the data using equations (3)–(5), resulting in the amplitude (strength) and direction of azimuthal variations in phase velocity (Figure 4) as well as the isotropic phase velocities (Figure 5). Strong azimuthal anisotropy from 5 to 7.5 s is observed with peak-to-peak amplitudes ranging

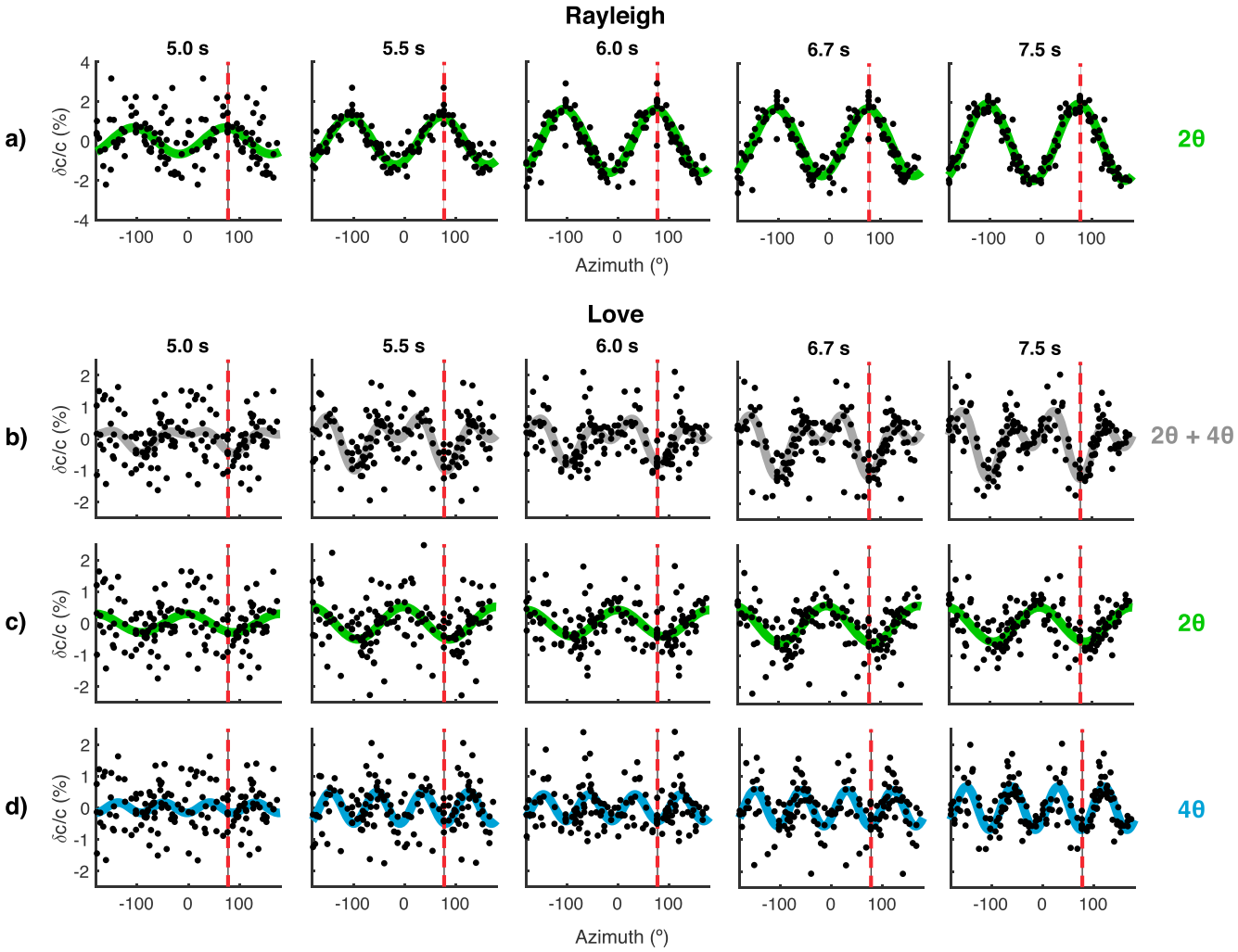

Figure 4. Azimuthal variation of phase velocity residuals relative to their isotropic values (see Figure 5 for the isotropic velocities, c_0) where 2θ, 4θ, and $2\theta + 4\theta$ sinusoidal fits are shown in green, blue, and gray, respectively. (a) Rayleigh wave 2θ; (b) Love wave $2\theta + 4\theta$; (c) Love wave 2θ only (4θ prediction subtracted from the observations); and (d) Love wave 4θ only (2θ prediction subtracted from the observations). The fossil-spreading direction (78°) is denoted by a red dashed line in each plot. To ensure high-quality data, only measurements from stations separated by ≥200 km are used. See Figures 9a and 9b for the anisotropy parameters (A, ψ) corresponding to each sinusoidal fit.

from 2% to 4% for Rayleigh-2θ and from 0.5% to 1% for both Love-2θ and Love-4θ (Figures 4 and 9a). The Rayleigh-2θ fast direction aligns parallel to the FSD. Additionally, the Love-2θ and Love-4θ fast directions approximately align with FSD+90° and FSD+45°, respectively. These inferred fast directions for Rayleigh and Love waves are consistent with predictions from Montagner and Nataf (1986) assuming FSD parallel anisotropic fabric. While Rayleigh and Love waves are both sensitive to the mantle, crust, and sediments at these periods (Figures 6a and 6b), the data clearly show a dominant signal consistent with strong mantle anisotropy oriented parallel to paleo-spreading, as observed previously at longer periods (Lin et al., 2016).

5. Inversion Methods

5.1. Radial Anisotropy

Isotropic phase velocity measurements for both Rayleigh and Love waves at 5–7.5 s (Figure 5) are used to constrain radial anisotropy in the upper ~35 km of the lithosphere. The inverse problem is parameterized in terms of the wave speeds of horizontally propagating vertically and horizontally polarized S waves (V_{SV}, V_{SH}) and vertically and horizontally propagating P waves (V_{PV}, V_{PH}) as well as η, which influences P-SV propagation at angles intermediate to vertical and horizontal but lacks a precise physical meaning (Kawakatsu, 2016a, 2016b). We choose to use the traditional η parameterization defined by Anderson (1961) instead of the newly defined η_κ, which has a clear physical meaning describing departures from the elliptic condition

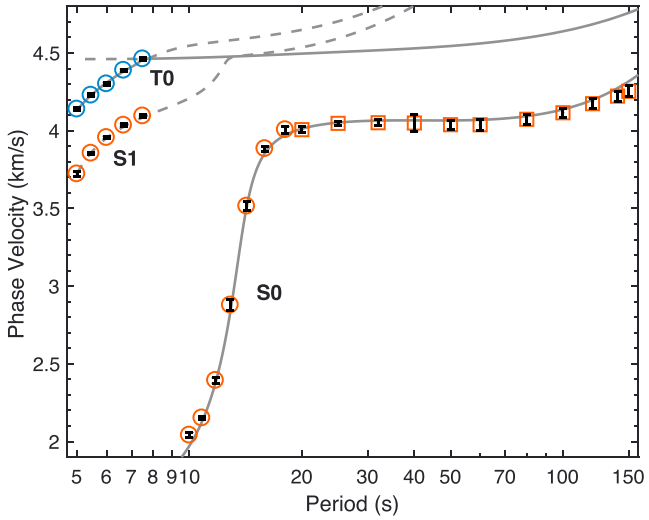

Figure 5. Isotropic phase velocity measurements, c_0, for the fundamental mode (S0) and first overtone Rayleigh waves (S1) in red and fundamental mode Love (T0) in blue. Measurements from 10–150 s are from Lin et al. (2016) and are included in the modeling for completeness. Ambient noise and teleseismic measurements are shown as circles and squares, respectively. Gray lines show the predictions of the preferred model from this study (model 3 in Figure 8) where the solid and dashed lines depict fundamental mode and first overtone predictions, respectively. Predicted phase velocities are corrected for physical dispersion using a reference frequency of 35 mHz (see Data Set S1 for anelastic Q model).

(Kawakatsu, 2016a, 2016b) but has yet to be applied to an inversion for Earth structure. Since η is poorly constrained by surface-wave data, we prescribe a character similar to that of PREM, whereby a linear gradient is imposed starting from 0.9 at the Moho to 1.0 at 200 km depth and is 1.0 elsewhere in the crust and upper mantle (Dziewonski & Anderson, 1981). The precise character of η beneath NoMelt may differ slightly from this assumption but is unlikely to have a significant effect on the resulting model. The equation linking observed isotropic phase velocities with the desired model parameters is expressed as

$$\begin{aligned}\delta c(\omega) &= \frac{c^2(\omega)}{U(\omega)} \int_a^0 \sum_i K_i(\omega, r)\, \delta m_i(r)\, dr \\ &= \frac{c^2}{U} \int_a^0 \left(K_{PV}\, \delta V_{PV}(r) + K_{PH}\, \delta V_{PH}(r) + K_{SV}\, \delta V_{SV}(r) \right. \\ &\qquad \left. + K_{SH}\, \delta V_{SH}(r) + K_\eta\, \delta \eta(r) \right) dr,\end{aligned} \tag{6}$$

where $\delta c(\omega) = c_0(\omega) - c^{pre}(\omega)$ is the residual between observed and predicted isotropic phase velocity for a given model iteration, $U(\omega)$ is group velocity, $K_m(\omega, r) = \omega^{-1} \cdot \partial\omega/\partial m$ are the eigenfrequency Fréchet derivatives for each model parameter (Figures 6a and 6b), and $\delta m = m - m_0^j$ are the model perturbations away from the starting model m_0 at iteration j. In matrix form, equation (6) becomes

$$\mathbf{K'}\left(\mathbf{m} - \mathbf{m}_0\right) = \delta \mathbf{c}, \tag{7}$$

where $\boldsymbol{K}' = \mathbf{K}\, c^2/U$ is the matrix of phase-velocity sensitivity kernels and $\mathbf{m}_0$ is the starting model from the previous iteration. In order to solve directly for $\mathbf{m}$, equation (7) can be rearranged:

$$\mathbf{K'}\,\mathbf{m} = \delta \mathbf{c'}, \tag{8}$$

where $\delta \boldsymbol{c}' = \delta \mathbf{c} + \boldsymbol{K}'\,\mathbf{m}_0$. Equation (8) allows for the straightforward implementation of constraint equations of the form $\mathbf{H}\,\mathbf{m} = \mathbf{h}$, applied directly to $\mathbf{m}$ as opposed to the model perturbations, $\delta\mathbf{m}$. Therefore, we have (Menke, 2012)

$$\begin{pmatrix} \mathbf{W}_e^{1/2}\mathbf{K'} \\ \mathbf{W}_\varepsilon^{1/2}\mathbf{H} \end{pmatrix} \mathbf{m} = \begin{pmatrix} \mathbf{W}_e^{1/2}\delta\mathbf{c'} \\ \mathbf{W}_\varepsilon^{1/2}\mathbf{h} \end{pmatrix}, \tag{9}$$

where $\mathbf{W}_e$ is a diagonal weighting matrix containing uncertainties in isotropic phase velocity, σ^{-2}, obtained from bootstrapping the sinusoidal fitting parameters in equations (3)–(5), and $\mathbf{W}_\varepsilon$ contains damping parameters for each constraint equation. Finally, the least squares solution, which minimizes the misfit function $\Phi = \left(\delta\mathbf{c'} - \mathbf{K'}\,\mathbf{m}\right)^{\mathrm{T}} \mathbf{W}_e \left(\delta\mathbf{c'} - \mathbf{K'}\,\mathbf{m}\right) + \left(\mathbf{h} - \mathbf{H}\,\mathbf{m}\right)^{\mathrm{T}} \mathbf{W}_\varepsilon \left(\mathbf{h} - \mathbf{H}\,\mathbf{m}\right)$, is given by

$$\mathbf{m} = \left(\mathbf{K'}^{\mathrm{T}} \mathbf{W}_e \mathbf{K'} + \mathbf{H}^{\mathrm{T}} \mathbf{W}_\varepsilon \mathbf{H} \right)^{-1} \left(\mathbf{K'}^{\mathrm{T}} \mathbf{W}_e \delta\mathbf{c'} + \mathbf{H}^{\mathrm{T}} \mathbf{W}_\varepsilon \mathbf{h} \right). \tag{10}$$

The inverse problem is solved iteratively by calculating $\mathbf{m}$, updating $\mathbf{m}_0$, and recalculating $\delta\mathbf{c}$ until the model converges and the change in misfit $\boldsymbol{\Phi}$ is small from one iteration to the next. Sensitivity kernels and predicted phase-velocity dispersion, c^{pre}, are calculated at each iteration using MINEOS with a physical dispersion correction using an assumed Q model (Data Set S1) and a reference frequency of 0.035 Hz. Due to the small array size relative to lateral velocity variations, we invert all available data for a single 1-D velocity profile representative of the entire NoMelt study region.

Inversions for mantle velocity structure are dependent on the starting crustal velocity model (Figures 6a and 6b). We use the average NoMelt P wave refraction model as the isotropic starting crustal V_{PV} and V_{PH} (Lizarralde et al., 2012) and convert to V_S using V_P/V_S of 1.85 from Brocher (2005). The starting crustal velocity model is shown in Figure 7 along with crust1.0 (Laske et al., 2013) and Lin et al. (2016) for comparison. We use a single sediment layer of 250-m thickness inferred from the refraction model and assign to it a constant shear velocity of 250 m/s (Ruan et al., 2014), which remains fixed throughout the inversion. Because

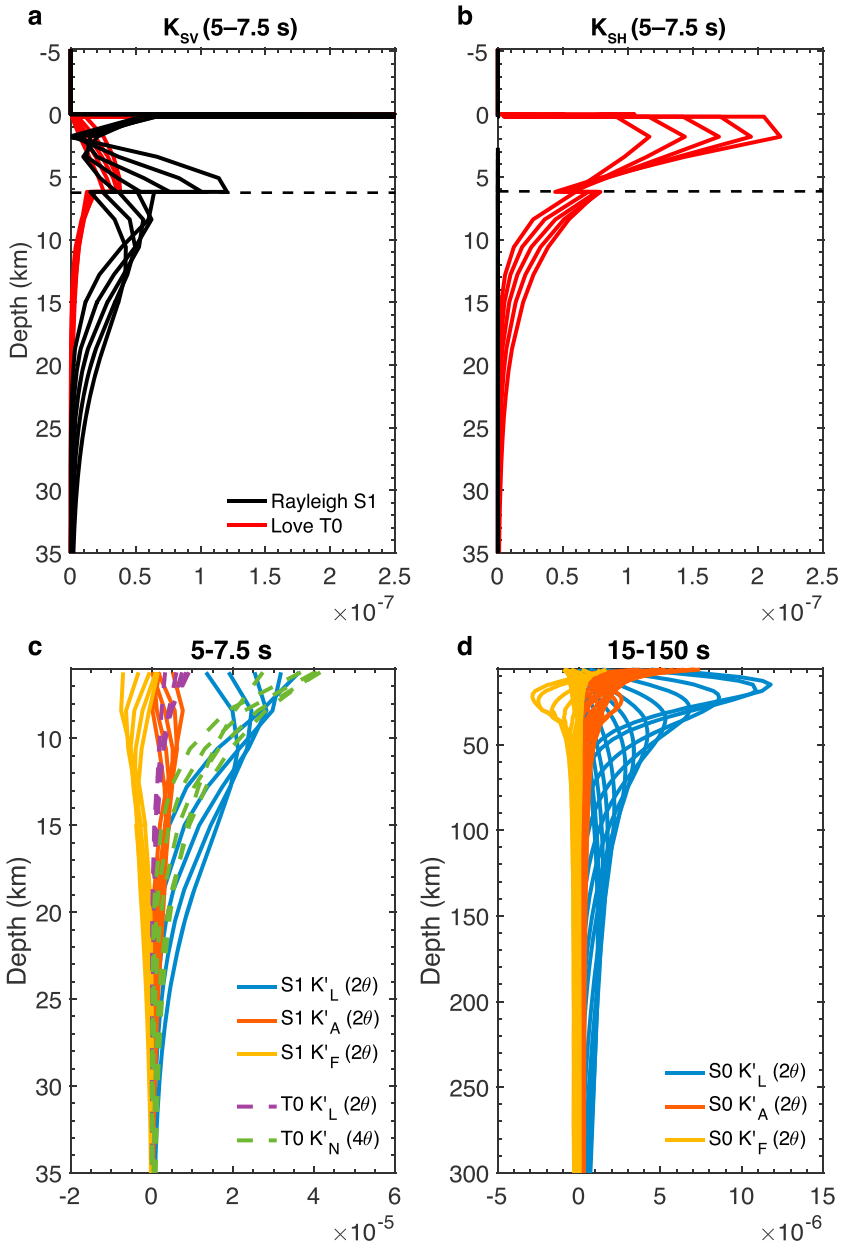

Figure 6. Phase velocity sensitivity kernels used in the radial and azimuthal anisotropy inversions. (a) V_{SV} model sensitivity to the first overtone Rayleigh (black solid) and fundamental mode Love waves (red) from 5 to 7 s. The Moho is marked by the black dashed line. (b) Same as (a) but for V_{SH} sensitivity. (c) Sensitivity to G (K_L), B (K_A), H (K_F), and E (K_N) from 5 to 7.5 s. Solid and dashed lines represent first overtone Rayleigh and fundamental mode Love-wave sensitivities, respectively. (d) Same as (c) but for fundamental mode Rayleigh-wave sensitivity to G, B, and H from 15 to 150 s.

V_{PV} and V_{PH} are difficult to resolve independently with surface-wave data, we instead allow V_{SV} and V_{SH} to vary and impose a constraint requiring the corresponding components of V_P to vary proportionally. The amount that V_P varies with V_S is determined by V_P/V_S of the starting model and remains fixed throughout the inversion. Additional damping toward the starting model ensures stability between iterations.

Borehole constraints show $V_{PH} \approx V_{PV}$ in the upper ~1.5 km (layer 2) of the oceanic crust (Swift et al., 1998); therefore, we require the upper 1.5 km of the crust to remain isotropic ($\xi = 1$) throughout the inversion. Variations of ξ with depth in the lower crust and mantle are not well resolved by our data set due to the narrow bandwidth of the high-frequency measurements and poor depth sensitivity of Love waves. Therefore,

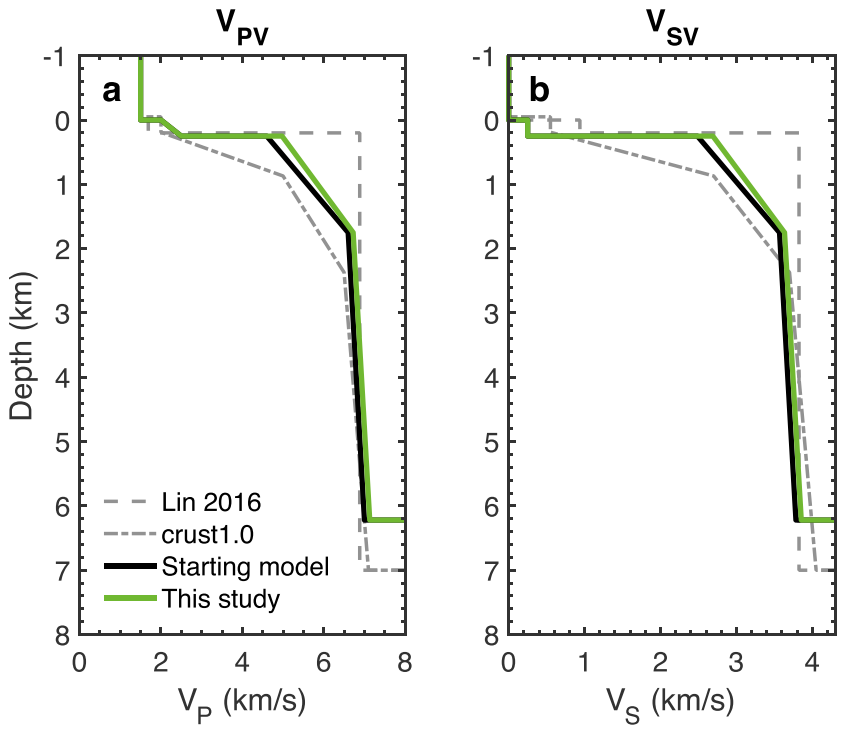

Figure 7. The radially isotropic ($V_{SH} = V_{SV}, V_{PH} = V_{PV}$) starting crustal model for (a) V_P and (b) V_S derived from the NoMelt P wave refraction study is shown in black. Velocity models from crust1.0 (Laske et al., 2013) and Lin et al. (2016) are shown for comparison. The final preferred model (V_{PV}, V_{SV}) of this study is shown in green (same as model 3 in Figure 8).

layers of constant radial anisotropy are enforced in the lower crust and mantle, respectively, by starting with an isotropic model and requiring constant $\partial\xi/\partial r$ within each layer (see Text S1). This constraint effectively reduces the number of model parameters such that additional smoothing is not required.

5.2. Azimuthal Anisotropy

The azimuthal variations of Rayleigh-wave (5–150 s) and Love-wave (5–7.5 s) phase velocities are inverted for depth-dependent anisotropy parameters $G_{c,s}$, $B_{c,s}$, and $H_{c,s}$ from the Moho down to 400 km depth and $E_{c,s}$ from the Moho to 35 km depth (~30 km depth beneath the Moho) following the formulation of Montagner and Nataf (1986). They show that the phase velocity sensitivities of the azimuthally anisotropic depth parameters equal the sensitivities of the corresponding transversely isotropic Love parameters. Thus, the Rayleigh-2θ, Love-2θ, and Love-4θ cosine and sine amplitude components are written in terms of the four desired anisotropic depth functions as

$$A^R_{c2,s2}(\omega) = \frac{c}{U}\int\left(LK^R_L\frac{G_{c,s}}{L}(r) + AK^R_A\frac{B_{c,s}}{A}(r) + FK^R_F\frac{H_{c,s}}{F}(r)\right)dr, \tag{11}$$

$$A^L_{c2,s2}(\omega) = \frac{c}{U}\int\left(-LK^L_L\frac{G_{c,s}}{L}(r)\right)dr, \tag{12}$$

$$A^L_{c4,s4}(\omega) = \frac{c}{U}\int\left(-NK^L_N\frac{E_{c,s}}{N}(r)\right)dr, \tag{13}$$

where K_A, K_L, K_F, and K_N are eigenfrequency Fréchet derivatives of the corresponding Love parameters, which depend on frequency ω and radius r. The preferred model from the radial anisotropy inversion (model 3 in Figure 8) is used to calculate the Fréchet derivatives and elastic constants. In matrix form, equations (11)–(13) become

$$\begin{pmatrix}\mathbf{A}^R_{c2,s2}(\omega)\\ \mathbf{A}^L_{c2,s2}(\omega)\end{pmatrix} = \begin{pmatrix}\mathbf{K'}^R_L(\omega,r) & \mathbf{K'}^R_A(\omega,r) & \mathbf{K'}^R_F(\omega,r)\\ \mathbf{K'}^L_L(\omega,r) & \mathbf{0} & \mathbf{0}\end{pmatrix}\begin{pmatrix}\mathbf{G}_{c,s}/\mathbf{L}(r)\\ \mathbf{B}_{c,s}/\mathbf{A}(r)\\ \mathbf{H}_{c,s}/\mathbf{F}(r)\end{pmatrix}, \tag{14}$$

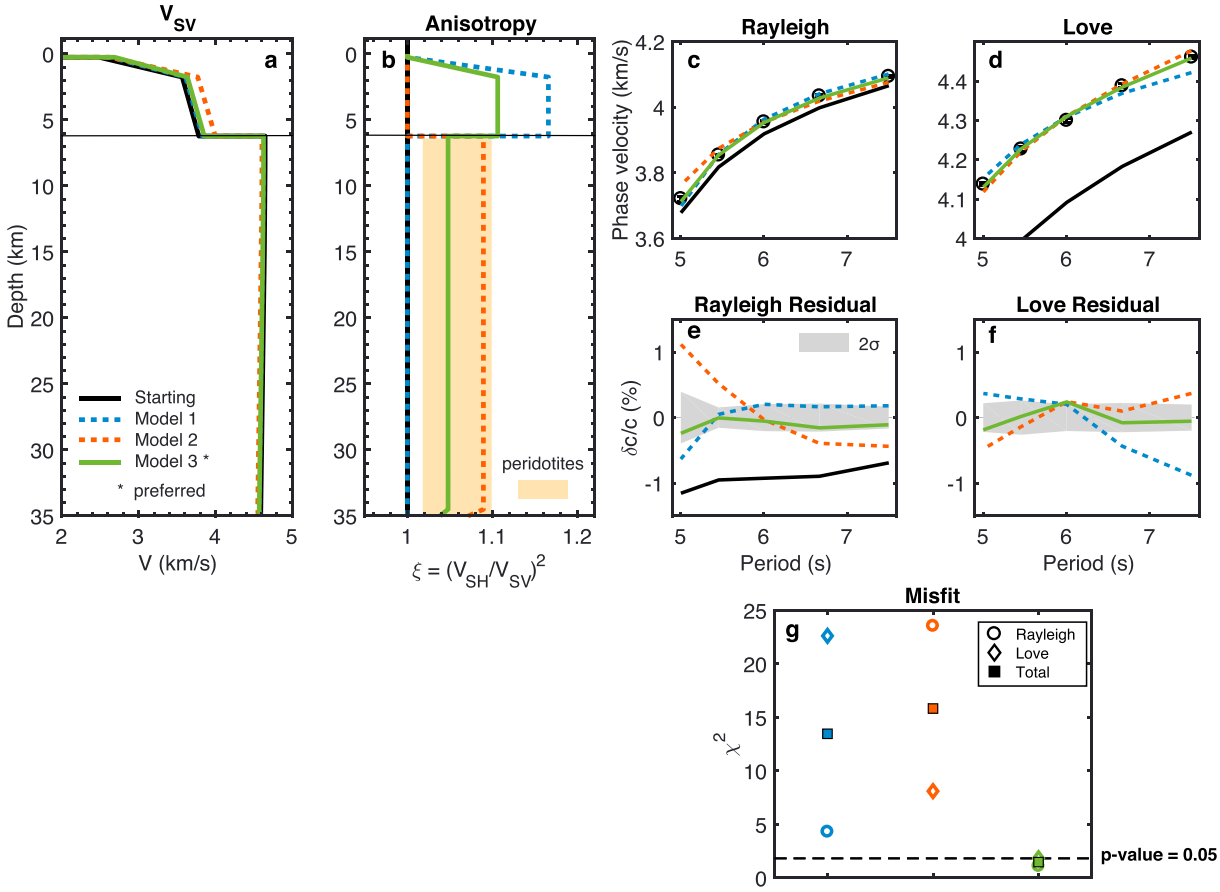

Figure 8. Radial anisotropy squeeze test: (a) V_{SV} and (b) radial anisotropy ξ of the starting model in black, plotted against Model 1 (anisotropic lower crust), Model 2 (anisotropic mantle), and Model 3 (anisotropic crust and mantle). The black thin line marks the Moho, and the orange bar shows ranges of ξ measured from peridotites from the Antalya ophiolite complex (lower bound; Peselnick & Nicolas, 1978) and from fast-spreading environments (upper bound; Ismail & Mainprice, 1998). (c and d) Calculated and observed Rayleigh- and Love-wave dispersion. (e and f) Rayleigh and Love phase velocity residuals with the 2σ measurement error shaded in gray, where negative values indicate phase velocities that are underpredicted. Love-wave residuals of the starting model range from −4% to −6% (beyond figure axis). (g) Reduced chi-square misfit of phase velocities for each model, defined as $\chi^2 = N^{-1}\sum_i^N (c_i^{obs} - c_i^{pre})^2/\sigma_i^2$. Models plotted above the black dashed line have a p value less than 0.05 and can be rejected with greater than 95% confidence. Model 3 (green solid) fits the Rayleigh- and Love-wave measurements to within 2σ, yielding the lowest overall misfit ($\chi^2 \approx 1$) and therefore is our preferred model.

$$\mathbf{A}^L_{c4,s4}(\omega) = \mathbf{K'}^L_N(\omega, r)\mathbf{E}_{c,s}/\mathbf{N}(r), \tag{15}$$

where boldface variables are vectors and $\mathbf{K'}_j = (c/U)j\,\mathbf{K}_j\,dr$ are matrices containing the scaled sensitivity kernels (Figures 6c and 6d).

Rayleigh waves are weakly sensitive to $B_{c,s}$ and $H_{c,s}$, which depend mostly on V_{PH} and η, respectively. Therefore, we use peridotites from the literature (i.e., Ismail & Mainprice, 1998; Peselnick & Nicolas, 1978) to enforce scaling relations between $B_{c,s}$, $H_{c,s}$, and $G_{c,s}$. The elastic tensors are rotated such that their inferred shear planes are horizontal (i.e., horizontal [100] crystallographic axes), and ratios G/L, B/A, and H/F are calculated from equations (A12)–(A17). This yields approximate scaling relations of $B_{c,s}/A = 1.25\,G_{c,s}/L$ and $H_{c,s}/F = 0.11\,G_{c,s}/L$, which are used as prior constraints in the inversion. Equations (14)–(15) are inverted using standard damped-weighted least squares with second derivative smoothing and a priori constraints forcing G, B, and H to zero below 300 km. The inversions are carried out using the cosine and sine representation of the anisotropy depth functions with the corresponding strengths and directions defined by equations (A8)–(A11).

In order to evaluate confidence in the final models, a balanced bootstrap resampling algorithm is used (Davison et al., 1986). Balanced resampling of M data over N iterations involves randomly selecting M points from the full data set allowing for repetition and requiring that every datum is eventually selected N times.

This method ensures even sampling over the entire data set with every point represented an equal number of times, reducing variance in bias and providing robust uncertainty estimates with fewer iterations compared to uniform resampling approaches (Hung et al., 2011). We perform 2,000 iterations of balanced resampling and calculate 68% (σ) and 95% (2σ) confidence bounds from the subset of final models, which fit the full data set with reduced chi-square less than 1.25 (1,424 models for G and 1,958 models for E).

6. Results

6.1. Radial Anisotropy

Azimuthally averaged high-frequency Love- and Rayleigh-wave dispersions are fit by introducing radial anisotropy in the lower crust and upper ~30 km of the mantle. We compare three models where we have allowed anisotropy to appear in different parts of the model in order to evaluate where, if at all, anisotropy is required by the data (Figure 8). In model 1, anisotropy is allowed only in the lower crust, while the mantle is forced to be isotropic ($\xi = 1$). Model 2 contains anisotropy in the mantle with isotropy enforced in the crust. In model 3, anisotropy is allowed in both the crust and mantle.

The resulting suite of inverse models is shown in Figure 8. Love-wave dispersion is fit best by models with radial anisotropy in the mantle with $\xi > 1$ ($V_{SH} > V_{SV}$) (Figure 8, models 2 and 3). Rayleigh waves are best fit by models with stronger crustal anisotropy with $\xi > 1$ (Figure 8, models 1 and 3). In particular, forcing the mantle to be isotropic (model 1) underpredicts Love-wave velocities at periods >6 s. An isotropic crust (model 2) overpredicts Rayleigh-wave velocities <6 s and underpredicts them >6 s. Figure 8g shows large reduced-χ^2 misfit for Love waves in model 1 and Rayleigh waves in model 2 resulting in large total misfits for both models (χ^2 much greater than 1).

In order to evaluate model significance, we test the null hypothesis that the data are sufficiently described by the model using a chi-square test for goodness of fit. The black dashed line in Figure 8g indicates a significance level (p value) of 0.05. Models with a high χ^2 misfit that plot above this line have $p < 0.05$, meaning that the null hypothesis, and thus the model, can be rejected with greater than 95% confidence (or in other words, there is less than a 5% chance that the model does sufficiently describe the data but that a statistically improbable departure of χ^2 has occurred). Models plotting below this line have $p > 0.05$, and thus, the null hypothesis cannot be rejected. Model 3, which has a low misfit ($\chi^2 = 1.48$) and is within the 95% confidence limit of model acceptance ($p = 0.14$), is our preferred model (see Figures S3–S6 for the comprehensive exploration of the model space).

Model 3 in Figure 8 consists of radial anisotropy with $V_{SH} > V_{SV}$ by 2-3% ($\xi \sim 1.05$) in the mantle and 4-5% ($\xi \sim 1.1$) in the crust. It fits both Rayleigh and Love dispersion data to within the 2σ error bounds and produces the lowest total misfit. The depth extent of radial anisotropy in the mantle is not well resolved by the data set due to the decay of V_S sensitivity with depth below the Moho (Figures 6a and 6b), and therefore, we favor a simple model with single layers of anisotropy in the crust and upper ~30 km of the mantle. Due to the loss of sensitivity with depth, we cannot rule out models with anisotropy confined to the upper 10–15 km of the mantle. Our model agrees well with the range of $\xi = N/L$ calculated from oceanic petrofabrics of Peselnick and Nicolas (1978) and Ismail and Mainprice (1998), as indicated by the orange bar in Figure 8b (see section 7.1). Rayleigh and Love wave data cannot be simultaneously satisfied by radial anisotropy only in the crust or only in the mantle. Instead, the data require both the crust and uppermost mantle to be radially anisotropic with $\xi > 1$.

6.2. Azimuthal Anisotropy

Figure 9 shows strength and azimuth of G and E in the upper mantle, which control 2θ and 4θ variations in phase velocity, respectively. B and H are constrained using the scaling relations from peridotites mentioned previously, and we find B/A of ~6% directly beneath the Moho, which agrees well with P_n anisotropy of 6.2% observed at NoMelt (Mark et al., 2017). Deeper estimates of B/A agree well with oceanic peridotites (section 7.1). Since B and H are simply scalar multiples of G/L, we simplify the remainder of the discussion by focusing only on features of G and E.

The strength of G increases with depth in the uppermost mantle lithosphere from ~4.5% at the Moho (~6 km) to ~6% at ~30 km depth, resulting in a positive gradient of 0.06–0.08% per kilometer. This increase in G strength with depth in the uppermost mantle is required by the high-frequency data and was not previously resolved by Lin et al. (2016). In contrast, E strength is not required to increase with depth, and

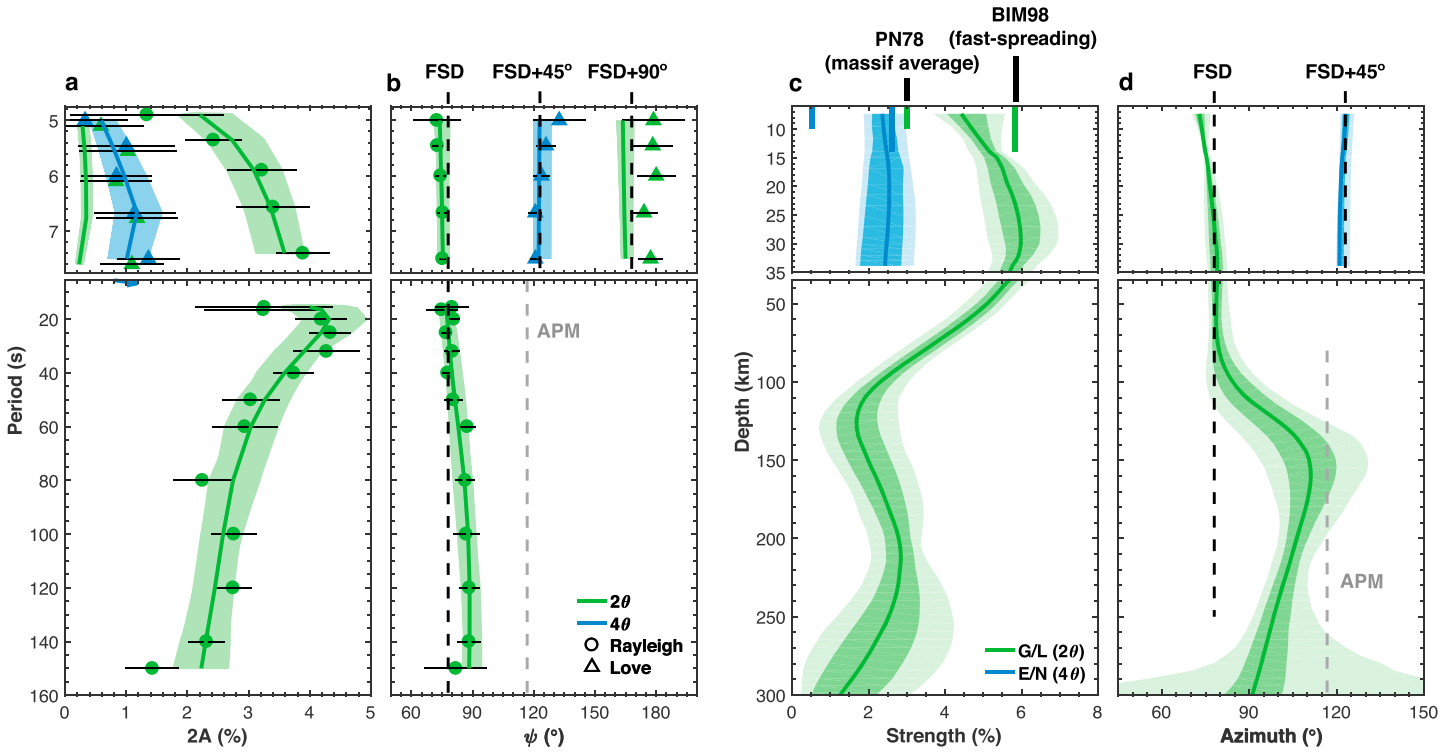

Figure 9. NoMelt azimuthal anisotropy data fit (a and b) and model (c and d). Measurements from 15 to 150 s are from Lin et al. (2016). Top panels have expanded vertical scales to highlight short-period data and upper-lithosphere models. (a) Peak-to-peak amplitudes of azimuthal anisotropy, $2A$, measured for each mode branch from Figure 4. 2θ and 4θ measurements are represented by green and blue symbols, respectively, and their 2σ errors by black solid bars. Rayleigh measurements are represented by circles and Love measurements by triangles. Thick solid lines show the median model predictions resulting from 2,000 bootstrap iterations, and shading represents the range of model predictions. (b) Same as (a) but for fast directions, ψ. The black dashed lines represent fast directions predicted for each wave type from Montagner and Nataf (1986) assuming olivine alignment parallel to the fossil-spreading direction (FSD) of 78°. The gray dashed line represents absolute plate motion (APM). (c) Strength of anisotropy parameters G/L and E/N are shown in green and blue, respectively. Petrofabric estimates from Peselnick and Nicolas (1978; Mesozoic ophiolite; labeled PN78) and Ismail and Mainprice (1998; fast-spreading peridotites; BIM98) are shown by short and long bars, respectively. The solid lines are the median model values obtained from bootstrapping, and light and dark shading depict the 95% and 68% confidence bounds, respectively. (d) Same as (c) but for anisotropy azimuth, Ψ.

we observe a relatively constant strength of 2–2.5% from the Moho down to 35 km depth. These magnitudes of G and E strength are consistent with petrofabrics from Peselnick and Nicolas (1978) and Ismail and Mainprice (1998; thick bars in Figure 9c; see section 7.1). Estimates from BIM98 coincide with our seismic observations of G/L from ~15–35 km depth and E/N from the Moho to 35 km depth to within the 68% confidence contours. Below ~35 km depth, G strength decreases, reaching a minimum of ~2% at ~135 km depth, which corresponds with the LVZ (Figure 11). This feature was previously seen by Lin et al. (2016) and interpreted as relatively weak fabric development within the center of a low viscosity asthenospheric channel with non-Newtonian rheology. Finally, there is a secondary peak in G strength of ~3% at 210–240 km depth that Lin et al. (2016) interpreted as strong fabric development at the base of an asthenospheric channel due to pressure- and/or buoyancy-driven flow.

We also solve for Ψ_G and Ψ_E in the upper 300 and 35 km, respectively. In the lithosphere, Ψ_G is parallel to the FSD to within ~7° and Ψ_E is 45° rotated from fossil spreading to within ~5°. The direction of G remains parallel to the FSD down to 80–90 km depth before rotating clockwise down to 150–160 km depth, approaching but never reaching the APM direction. Deeper in the model, anisotropy rotates back counterclockwise and is neither parallel to FSD nor APM, as observed previously (Lin et al., 2016).

Although the model presented here fits the Rayleigh-2θ and Love-4θ data to within measurement error, the Love-2θ measurements are not well fit (Figures 9a and 9b). In particular, the G model predicts a Love-2θ direction that is 10–15° counterclockwise from the true measurements. Additionally, the strength of the Love-2θ component is underestimated by a factor of 2–4. Since these are some of the first robust in situ

Table 1
C_{ij} Constructed at 30 km Depth Beneath NoMelt and Rotated Into the (x'_1, x'_2, x'_3) Coordinate System With C_{45}, C_{16}, C_{26}, and C_{36} Minimized

i	j	1	2	3	4	5	6
1		271.6149	101.6837	101.2700	0	0	−0.1902
2		—	233.9946	99.9429	0	0	0.3918
3		—	—	239.5542	0	0	0.0071
4		—	—	—	66.1769	0.0452	0
5		—	—	—	—	74.6177	0
6		—	—	—	—	—	71.9655

Note. See main text; rotation angle is 78.3°. x'_1 is parallel to the [100] crystallographic axis and x'_3 vertical. Units are GPa and the lower diagonal terms have been omitted ($C_{ij} = C_{ji}$).

measurements of the full Love-2θ/-4θ behavior, further modeling efforts are required to fully understand the source of these discrepancies (see section 7.2.3).

7. Discussion

7.1. Comparison to Petrofabrics

Elastic properties of peridotites gathered in the field provide direct constraints on upper mantle fabric, and because they have traveled to the surface, these samples are thought to be most representative of shallow mantle lithosphere. However, many seismic models constructed from global data sets have relatively poor shallow resolution, making direct comparisons with natural samples unfeasible. Our model provides some of the first high-resolution constraints on shear-wave anisotropy of the lithosphere, allowing for direct comparisons with peridotites. Although measurements on petrofabrics may be performed at different P-T conditions than occur in the mantle, the anisotropic components depend only on relative differences in elements of the elastic tensor (Ismail & Mainprice, 1998), and to first order, direct comparisons with our model can be made without the need for pressure and temperature corrections.

We compare the anisotropic structure observed at NoMelt with elastic tensors (C_{ij}) representing average oceanic upper mantle from two petrofabric studies: (1) an average of 72 olivine aggregates of peridotites from fast-spreading environments by Ismail and Mainprice (1998; BIM98) and (2) an outcrop-scale massif average of the Antalya ophiolite complex representative of Mesozoic uppermost oceanic mantle by Peselnick and Nicolas (1978; PN78), as well as the single harzburgite sample used to construct that average. The averaging procedures between the two studies are quite different. BIM98 determine the structural fabric (lineation direction and pole to foliation plane) for each of the 72 samples and orient them in a consistent framework before averaging them together. In contrast, PN78 utilize ultrasonic measurements from cores of a single harzburgite sample in addition to 100 field observations of the structural fabric as it appears today to reconstruct a massif average C_{ij} for the Antalya ophiolite complex. Since the integrity of the PN78 massif average relies heavily on the single harzburgite sample used to construct the average, we include it also in our comparisons.

The anisotropic elasticity tensor, C_{ij}, is calculated for the NoMelt model at 30 km depth containing all 13 elements in equation (A23). The resulting C_{ij} is oriented with its *SV* fast axis ([100]) in the direction of fossil spreading, rotated ~78° clockwise from x_1 and within the horizontal $x_1 - x_2$ plane. For ease of comparison with BIM98 and PN78, we rotate the coordinate system about x_3 to form a new system (x'_1, x'_2, x'_3) in which the [100] crystallographic axis is aligned parallel to x'_1 (Table 1; see Figure 10 for diagram of coordinate system). This is achieved by rotating the $x_1 - x_2$ coordinate axes clockwise about x_3 until the C_{ij} elements associated with G_s, B_s, H_s, and E_s are minimized (i.e., minimizing the function $\lambda = \sqrt{C_{45}^2 + C_{36}^2 + C_{16}^2 + C_{26}^2}$). The optimal rotation occurs at ~78.3° and is the inferred FSD at 30 km depth beneath NoMelt. Equations (A20)–(A22) are solved along all azimuths in the horizontal x'_1–x'_2 plane, yielding the velocities and polarizations of three orthogonal waves: the quasi *P* wave (V_{qP}), quasi-horizontal *S* wave (V_{qSH}) polarized approximately in the x'_1–x'_2 plane, and quasi-vertical *S* wave (V_{qSV}) polarized approximately in the x'_1–x'_3 plane (Crampin, 1981).

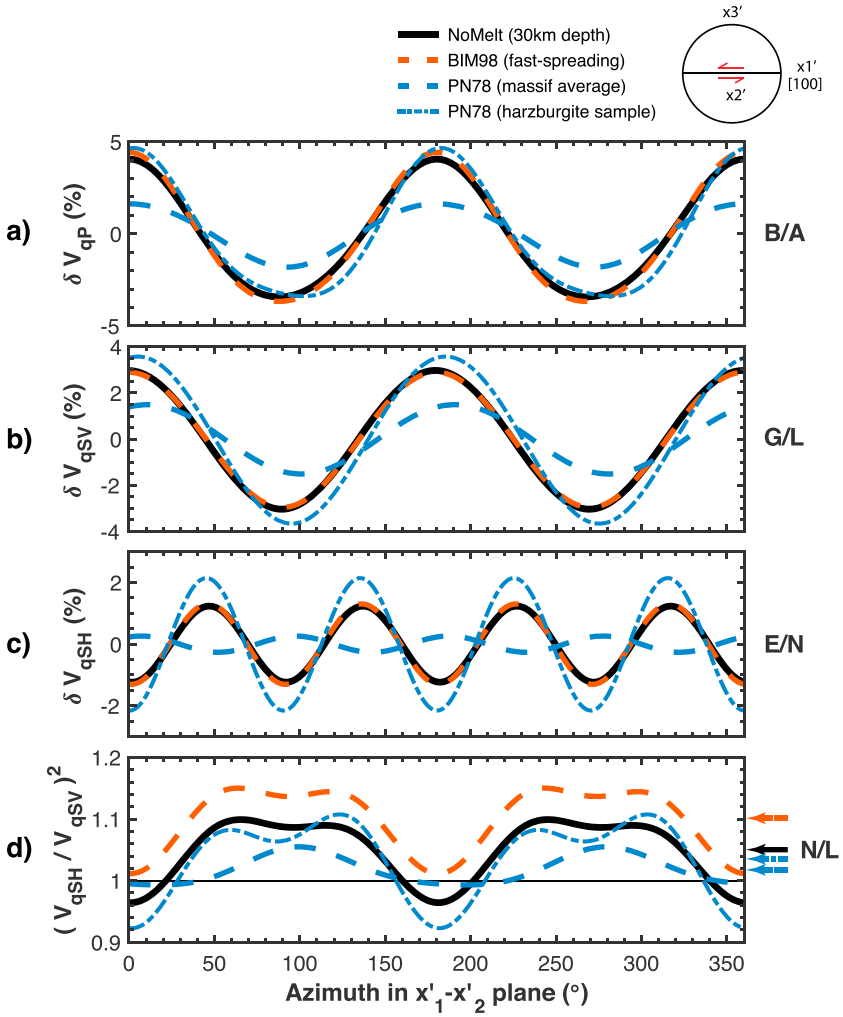

Figure 10. Azimuthal anisotropy is calculated from the NoMelt C_{ij} at 30 km depth (Table 1) and compared to BIM98 (Ismail & Mainprice, 1998) and PN78 (Peselnick & Nicolas, 1978) for (a) δV_{qP}, (b) δV_{qSV}, (c) δV_{qSH}, and (d) $(V_{qSH}/V_{qSV})^2$. The peak-to-peak variations in (a), (b), and (c) correspond to B/A, G/L, and E/N, respectively. The azimuthal average of (d) corresponds to ξ and is shown as an arrow at the right of the plot for each tensor. All tensors are oriented such that the shear plane is defined by x'_1–x'_2 with shear in the x'_1 direction. The NoMelt tensor has been rotated counterclockwise about the x_3 (vertical) axis by 78.3° such that the fast [100] axis is along x'_1. Zero azimuth is parallel to x'_1.

Figure 10 shows the predicted azimuthal (δV_{qP}, δV_{qSV}, δV_{qSH}) and apparent radial (V^2_{qSH}/V^2_{qSV}) anisotropy for each C_{ij}. Each tensor is oriented such that its shear plane is horizontal (x'_1–x'_2 plane) with shear in the direction of x'_1. The NoMelt P wave anisotropy, δV_{qP}, is $\sim$ $1.25\delta V_{qSV}$ as a result of the scaling enforced between B and G in the inversion. For NoMelt, we predict V_{qSV} anisotropy of ~6% peak-to-peak with a fast direction in the x'_1 ([100]) direction, in agreement with G/L (Figure 9). Similarly, we predict peak-to-peak V_{qSH} anisotropy of ~2.5% with a fast direction 45° rotated from the x'_1 direction, consistent with E/N. For radial anisotropy (the azimuthal average of the squared wave speed ratio), we calculate $\xi \sim 1.05$ or $V_{qSH} > V_{qSV}$ by ~2.4% (black arrow in Figure 10d).

In general, the mantle anisotropy measured in situ at NoMelt agrees with the petrofabrics that represent average oceanic upper mantle. The peak-to-peak amplitude and fast directions of P and S wave azimuthal anisotropy at NoMelt agree extremely well with BIM98, including the 4θ signal for δV_{qSH}. The BIM98 average displays very strong anisotropy since each of the 72 samples was rotated to its optimal orientation before being averaged, implying that the fabric at NoMelt is exceptionally coherent. Radial anisotropy at NoMelt is significantly weaker than BIM98, however, and agrees more closely with the PN78 harzburgite sample.

The PN78 massif average shows weaker radial and azimuthal anisotropy than what we observe and has a 4θ δV_{SH} signal that is $\sim 45°$ rotated.

One way to explain the relatively weak radial anisotropy and strong azimuthal anisotropy that we observe is by an LPO fabric other than perfectly horizontal A type (Karato et al., 2008). Horizontal shearing to produce an A-type fabric results in horizontal [100] (fast) axes parallel to the shear direction and vertical [010] (slow) axes perpendicular to the shear plane (i.e., activation of the [100](010) slip system), producing relatively strong radial anisotropy and weaker azimuthal anisotropy. However, the same deformation in an E-type regime activates the [100](001) slip system producing subhorizontal alignment of both [100] and [010] with vertical [001] (intermediate) axes, resulting in strong azimuthal anisotropy and relatively weak radial anisotropy, similar to what we observe. Weak radial anisotropy can also result from A-type fabric that has been rotated about x_2 such that the [100] axis is tilted from the horizontal plane. The PN78 harzburgite is an example of such a fabric with [100] rotated $\sim 20°$ out of the foliation plane and agrees with the radial anisotropy that we observe quite well, although E/N is overestimated. Such rotated fabrics are commonly observed in natural (Warren et al., 2008; Webber et al., 2010) and laboratory (Skemer et al., 2011; Zhang & Karato, 1995) olivine samples as well as in numerical models of fabric development (Blackman & Kendall, 2002b, 2002a; Blackman et al., 2017, Kaminski & Ribe, 2001) and may be linked to deformation history or preexisting LPO fabrics (Skemer et al., 2012). Forward calculations suggest that BIM98 fabric with the fast direction rotated $\sim$25° from the horizontal plane produces azimuthal and radial anisotropy that are very similar to the NoMelt model. We prefer this interpretation given that E-type fabric implies higher water content than typically expected for a MOR environment (e.g., Jung et al., 2006; Karato et al., 2008).

We have no need for alternative mechanisms for anisotropy such as diking, layering, or other shape-preferred orientations (e.g., Backus, 1962; Holtzman & Kendall, 2010). Laminate structures proposed to explain high-frequency scattered phases (P_n and S_n) in western Pacific lithosphere (Kennett & Furumura, 2013; Kennett et al., 2014; Shito et al., 2013, 2015) would produce strong apparent radial anisotropy with $\xi > 1$ and weak (negligible) azimuthal anisotropy, the opposite of that observed here. If such structures are present in the NoMelt region, either the velocity heterogeneity must be weak enough to produce relatively minor contributions to radial anisotropy, or they must exist below $\sim$30 km depth.

7.2. Comparison to Previous Pacific Studies

Efforts to model seismic anisotropy in the Pacific basin range in scale from global surface-wave studies to active-source refraction experiments. Long-period surface waves that traverse the plate are broadly sensitive to both the lithosphere and asthenosphere, providing a plate-scale view of seismic anisotropy and mantle flow, while active-source experiments utilizing P_n waves sample the local lithospheric structure just beneath the Moho. Although complimentary, these two types of observations lack the overlapping sensitivities (both laterally and in depth) required to constrain the complete anisotropic structure. Furthermore, agreement between recent global and regional models of radial and azimuthal anisotropy is relatively poor, especially at lithospheric depths. Local-scale broadband OBS array deployments like NoMelt bridge the gap between these existing data sets by providing local, high-frequency surface wave constraints on shear anisotropy in the shallow lithosphere. Here we compare our results with previous Pacific models of seismic anisotropy that range from global- to regional-scale, focusing primarily on lithospheric anisotropy.

7.2.1. Global and Plate-Scale Models

The fast propagation direction of Rayleigh-waves, Ψ_G, is a proxy for the direction of shear strain in the mantle and is typically thought to be parallel to the FSD in the oceanic lithosphere (Nicolas & Christensen, 1987). While many seismic observations in the Pacific support this notion (e.g., Beghein et al., 2014; Debayle & Ricard, 2013; Eddy et al., 2018; Forsyth, 1975; Forsyth et al., 1998; Hess, 1964; Lin et al., 2016; Nishimura & Forsyth, 1989; Raitt et al., 1969; Smith et al., 2004; Weeraratne et al., 2007), other observations of fast wave speeds rotated from fossil spreading in the lithosphere challenge this simple model of spreading-controlled fabric (Keen & Barrett, 1971; Morris et al., 1969; Shintaku et al., 2014; Takeo et al., 2016, 2018; Toomey et al., 2007, Vanderbeek & Toomey, 2017). Additionally, some global studies suggest that the correlation between Ψ_G and fossil spreading breaks down for older aged seafloor (Debayle & Ricard, 2013), perhaps due to reheating processes at >80 Ma (Becker et al., 2014). Becker et al. (2014) observe a spreading-rate dependence, where fast-spreading plates (>5 cm/year) display more coherent fossil-spreading parallel fabric compared to slower spreading. They also note that variations in Ψ_G between different seismic models are often greater than variations between seismic models and geodynamic models, suggesting the need for higher-resolution seismic constraints. Our broadband Rayleigh-wave measurements (5–150 s) require Ψ_G parallel to fossil spreading

within the lithosphere down to 80–90 km depth, followed by a rotation toward, but not parallel to, the plate-motion direction, perhaps signifying the transition to asthenospheric flow marking the approximate depth to the lithosphere-asthenosphere boundary (LAB) beneath NoMelt.

Estimates of the strength of G and its depth dependence vary widely between studies of different scales. Global studies using Rayleigh waves that traverse the basin observe stronger G in the asthenosphere relative to the lithosphere (Beghein et al., 2014; Burgos et al., 2014; Debayle & Ricard, 2013; Schaeffer et al., 2016; Yuan & Beghein, 2013), typically ranging in the lithosphere from 1% to 2% and from 3% to 3.5% in the asthenosphere, significantly weaker than oceanic petrofabrics (Figure 10). However, regional studies using data, which average over smaller regions of the plate, tend toward stronger anisotropy in the lithosphere relative to the asthenosphere (Lin et al., 2016; Nishimura & Forsyth, 1989; Rychert & Harmon, 2017; Takeo et al., 2016) as well as stronger anisotropy overall. We invert for all six parameters (G, Ψ_G, B, Ψ_B, H, and Ψ_H) controlling 2θ Rayleigh-wave variations and observe strong G in the lithosphere of 4–6% that weakens into the asthenosphere (2–3%), generally in agreement with other regional-scale studies but ~2–3 times stronger in the lithosphere than global studies. We also observe a positive gradient in G with depth in the lithosphere that is constrained by the short-period data, not previously seen by Lin et al. (2016). Although evidence of a positive lithospheric gradient in G can perhaps be seen in some studies (e.g., Nishimura & Forsyth, 1989; Rychert & Harmon, 2017; Yuan & Beghein, 2014), it has not been interpreted. We discuss this gradient in relation to numerical models of fabric formation at the MOR in section 7.3.

Several factors contribute to variations in G strength. The strength of azimuthal anisotropy has been shown to vary with spreading rate (Gaherty et al., 2004; Song & Kim, 2011) as well as plate age (Eddy et al., 2018; Smith et al., 2004), and the direction of the anisotropy can vary rapidly due to abrupt changes in spreading history. It is widely observed that the fossil-spreading history of the Pacific is complex, resulting in relatively short-wavelength changes in fast direction. These variations are difficult to resolve tomographically, and the resulting models are likely to underestimate the strength of the fabric (e.g., Nishimura & Forsyth, 1989). In contrast, anisotropy induced by APM is highly coherent and smooth over the scale of the Pacific basin, and its strength is likely to be well resolved by large-scale models. Our result suggests that at the local scale, mantle deformation in the ocean basins is dominated by flow associated with seafloor spreading and that subsequent deformation in the asthenosphere, including shear induced by APM, are secondary processes in comparison.

Our preferred model of radial anisotropy shows $\xi > 1$ in both the lower crust and lithospheric mantle. Figure 11 compares isotropic shear velocity and radial anisotropy for several recent regional and global models roughly within the NoMelt footprint. While V_{SV} estimates agree relatively well at most depths, ξ does not, particularly in the lithosphere. Global models tend to show $\xi < 1$ (Beghein et al., 2014; Burgos et al., 2014; Kustowski et al., 2008; Moulik & Ekström, 2014; Nettles & Dziewoński, 2008) in the lithosphere, at odds with our results and suggesting vertical fabric rather than horizontal. $\xi < 1$ has been observed in regions of upwelling such as beneath the EPR (e.g., Kustowski et al., 2008; Panning & Romanowicz, 2006) and is interpreted as vertical flow. However, it is more difficult to explain vertical fabric recorded in the oceanic lithosphere far from the ridge. Our results are instead consistent with regional models, which show $\xi > 1$ in the lithosphere (Forsyth, 1975; Gaherty et al., 1996; Nishimura & Forsyth, 1989; Tan & Helmberger, 2007; Takeo et al., 2013; Rychert & Harmon, 2017), indicating quasi-horizontal fabric consistent with numerical predictions of strain induced by corner flow at the ridge (e.g., Blackman & Kendall, 2002a). Some global models do observe $\xi > 1$ in the lithosphere (French & Romanowicz, 2014; Dziewonski & Anderson, 1981; Panning & Romanowicz, 2006), in agreement with our results. Our observations of ξ in the lithosphere are significantly weaker than observed previously (Figure 11b), perhaps due to the requirement of anisotropy in the crust.

The importance of accurate shallow estimates of radial and azimuthal anisotropy and their depth dependence has become increasingly clear. The relative strengths of ξ and G may help differentiate between different LPO fabric types, which reflect in situ temperature, stress, and water content (Jung & Karato, 2001; Karato et al., 2008). For example, typical A-type fabric should produce strong ξ and relatively weak G, while E type should exhibit weaker ξ relative to G. Additionally, the maximum of the gradient in radial anisotropy with depth ($\partial\xi/\partial r$) as well as the maximum gradient in fast-direction rotation ($\partial\Psi_G/\partial r$) have previously been used as proxies for depth to the LAB or G-discontinuity (e.g., Beghein et al., 2014; Burgos et al., 2014). However, the practice of using such depth derivatives of elastic parameters from global models to infer phys-

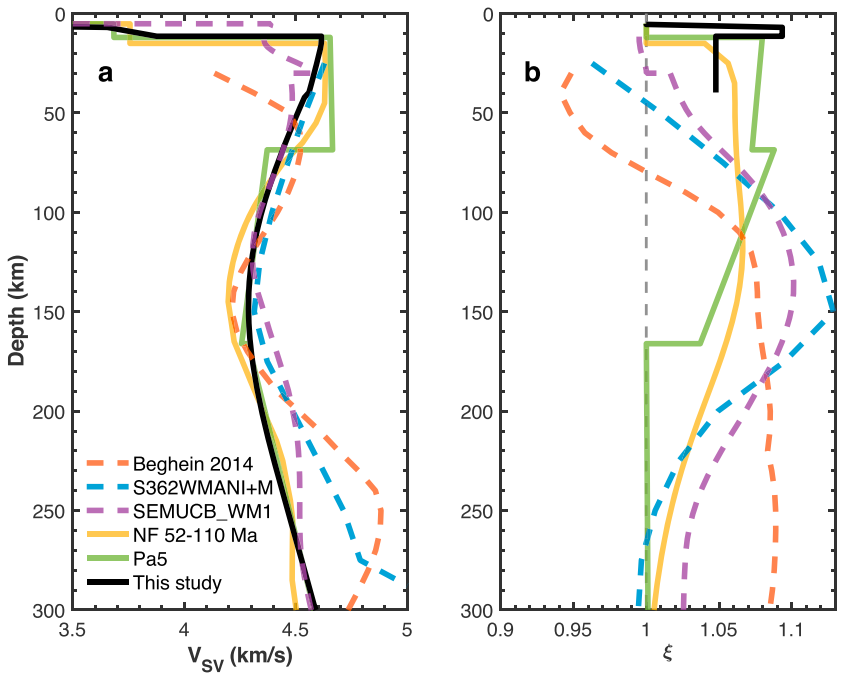

Figure 11. (a) Vertical shear velocity (V_{SV}) and (b) radial anisotropy (ξ) are compared for several regional and global models, each roughly within the NoMelt footprint. Regional models are shown as solid lines with Nishimura and Forsyth (1989) in yellow, Gaherty et al. (1996) in green, and the preferred model from this study in black (Figure 8, model 3). Dashed lines depict global models with Beghein et al. (2014) in red, Moulik and Ekström (2014) in blue, and French and Romanowicz (2014) in purple.

ical properties of the mantle should be performed with caution, and regional constraints should be utilized where possible (e.g., Kawakatsu & Utada, 2017; Takeo et al., 2018).

The relatively strong radial and azimuthal anisotropy observed in the lithosphere at NoMelt and other regional-scale studies compared to recent global studies is perhaps due to differences in sensitivities of the data sets used. Longer period surface waves have broad depth sensitivity that will necessarily smear shallow and/or thin layers of anisotropy. Thus, strong fabric that is shallow and/or has a fast direction rotated from the layers beneath it may appear weaker to longer period waves. Additionally, plate-scale studies utilizing Rayleigh waves that traverse large transects of the basin inherently average over heterogeneities that vary over short length scales. This may result in weaker estimates of G, especially if Ψ_G also varies appreciably. These depth and lateral limitations call for higher-frequency surface-wave constraints measured over smaller regions of the plate.

7.2.2. Ocean-Bottom Array Studies

In an effort to image upper mantle anisotropy in more detail, several other array-scale OBS surface-wave investigations have been carried out in various regions of the Pacific ranging in seafloor age from young (20–30 Ma; Shikoku basin; Takeo et al., 2013) to intermediate (60 Ma; TIARES project SE of Tahiti; Takeo et al., 2016) to old (130–160 Ma; PLATE and NOMan projects in the NW Pacific; Takeo et al., 2014, 2018). These studies utilize similar array-based techniques to model short-period surface-waves overlapping in sensitivity with our study and provide complementary constraints on both radial and azimuthal anisotropy that can be compared with our results. In detail, considerable heterogeneity exists in both radial and azimuthal anisotropy for different regions of the Pacific basin.

Strong radial anisotropy is observed in some areas of the Pacific, while others require none at all. Beneath the Shikoku basin, Takeo et al. (2013) observe a constant layer of anisotropy from the Moho to 220 km depth with V_{SH} faster than V_{SV} by 4–5% ($\xi = 1.083$ to 1.1052). In contrast, an isotropic uppermost mantle (upper 25 km) sufficiently explains Rayleigh- and Love-wave observations from 3- to 40-s period beneath the PLATE experiment (Takeo et al., 2014). Our preferred model requires strong radial anisotropy in the lower crust with V_{SH} faster than V_{SV} by 4-5% ($\xi \sim 1.11$) and relatively weak anisotropy of 2-3% ($\xi \sim 1.05$) in the upper ~30 km of the mantle. This strong crustal anisotropy suggests horizontal fabric that has not

been previously required by Pacific models but is consistent with proposed mechanisms of crustal accretion (see section 7.4). Our ability to resolve radial anisotropy in the crust is perhaps due to the relatively small lateral variations in crustal thickness across the NoMelt region, the small footprint and dense station spacing, and/or the accurate crustal starting model constrained by the P_n refraction study (Lizarralde et al., 2012). The radial anisotropy observed in the lithosphere beneath NoMelt is significantly weaker than in previous models (Figure 11b), perhaps due to our improved sensitivity to the crust. Forcing the crust to be isotropic produces ~4.4% ($\xi = 1.09$) radial anisotropy in the uppermost mantle, closer to previous models; however, the Rayleigh waves are not well fit in this case (model 2; Figure 8e). We are unable to constrain the depth dependence of ξ due to the limited depth-resolution of Love waves in the period band of 5–7.5 s (Figure 6b), and thus, longer period teleseismic Love-wave measurements are required.

Azimuthal anisotropy in the lithosphere also varies considerably in strength and direction across these focused regions of the Pacific basin. We find a positive gradient with depth in the lithosphere with a peak of ~6% G/L at ~30 km depth with a fast direction parallel to the FSD. In comparison, Takeo et al. (2014) observe stronger Rayleigh-wave anisotropy of 7% (assumed P wave anisotropy B/A of 9%) from the Moho to 60 km depth with a fast direction parallel to the FSD. Their single-layer model does not include H and underpredicts peak-to-peak amplitudes shorter than 6 s by 1–2%, suggesting a shallow layer of even stronger anisotropy. Beneath the TIARES region, Takeo et al. (2016) invert for G without accounting for B and H and find significantly weaker Rayleigh-wave anisotropy of ~3.5% in the lithosphere, which decreases to ~2% in the asthenosphere. Notably, the fast direction of anisotropy in the lithosphere is rotated 50–55° from fossil spreading, parallel to the direction of ancient plate motion prior to 43 Ma with a spreading rate of 2–3 cm/year. Their resolution tests are unable to recover structure shallower than 20 km depth, suggesting that if fossil-spreading parallel fabric does in fact exist, it must be embedded in the upper 20 km of the mantle. We observe Ψ_G parallel to fossil spreading from the Moho down to 80–90 km depth, significantly deeper for similarly aged lithosphere. This difference in fabric direction is perhaps related to the faster spreading rates inferred at NoMelt (4-5 cm/year) relative to TIARES (see section 7.3; Müller et al., 2008). At the NOMan region, Takeo et al. (2018) also observe significant Ψ_G rotation (~70°) away from fossil spreading at ~140-Ma lithosphere, perhaps associated with the complex triple paleo-ridge configuration. Less prominent rotations away from the spreading direction have also been observed in P_n refraction studies at the East Pacific Rise (~10°; Toomey et al., 2007), Juan de Fuca ridge (~18°; Vanderbeek & Toomey, 2017), as well as old seafloor in the western Pacific (10–15°; Shintaku et al., 2014), suggesting that modification of lithospheric fabric by underlying mantle flow is perhaps not uncommon.

7.2.3. Love-Wave Anisotropy

Previous observations of 4θ Love-wave anisotropy are scarce and comprised primarily of higher-mode data sets with broad depth sensitivities and very little discussion of their directional and amplitude variations (Montagner & Tanimoto, 1990, 1991; Trampert & van Heijst, 2002; Visser et al., 2008). Observations in the Pacific of 4θ variations in P_n (Shintaku et al., 2014; Mark et al., 2017) show fast directions quasi-parallel (and perpendicular) to fossil spreading, consistent with Love-wave fast directions rotated by 45° relative to fossil spreading in the shallow mantle. Our Love-4θ measurements are characterized by a peak-to-peak strength of 0.5–1.5% and a fast direction 45° rotated from FSD, in agreement with P_n anisotropy. Only two previous studies, that we are aware of, have inverted Love-4θ measurements for E (Trampert & van Heijst, 2002; Yuan & Beghein, 2014); both are global inversions which restrict their interpretations of E strength to the deep upper mantle and transition zone and do not interpret Ψ_E beyond noting disagreement between studies. We provide the first high-resolution estimates of E in the lithosphere with a strength of 2–2.5% and a direction 45° rotated from fossil spreading, in agreement with petrofabrics (Figures 9 and 10c).

In an anisotropic medium, the 2θ Love-wave variations should be small in magnitude compared to the 4θ variations (Montagner & Nataf, 1986). For this reason, Love-2θ is often thought to be negligible and has only been observed in a few previous studies (Forsyth, 1975; Montagner & Tanimoto, 1990, 1991; Visser et al., 2008). Rayleigh-Love coupling was speculated to cause this stronger-than-expected Love-2θ signal observed in some studies (Montagner & Tanimoto, 1990, 1991; Visser et al., 2008) and has been shown to produce strong Love-wave sensitivity to B and H in near-source regions (Sieminski et al., 2007). However, previous studies invariably find ψ_2^L parallel to FSD (and, therefore, parallel to ψ_2^R), perpendicular to predictions by Montagner and Nataf (1986) and Montagner and Anderson (1989) for an anisotropic medium with orthorhombic symmetry. We observe the first high-resolution Love-2θ signal with a fast direction that is perpendicular to FSD, in agreement with petrologic predictions. However, its strength is comparable to

that of the Love-4θ component, which is stronger than predicted and not fit by our model. We observe this strong 2θ component even when allowing for 2-D variations in isotropic phase velocity, suggesting that this signal is not due to unaccounted-for 2-D isotropic structure (Figure S2). Rayleigh-Love coupling (Love-wave sensitivity to B and H) may account for our unusually strong Love-2θ observations, but further investigation into coupling effects on Love-wave anisotropy at short periods is required.

7.3. Constraints on MOR Dynamics

As young oceanic lithosphere forms and cools away from the ridge, the mantle flow history is recorded in the LPO fabric of the lithosphere (Nicolas & Christensen, 1987). Therefore, observations of present-day radial and azimuthal anisotropy in the lithosphere are important for understanding ridge dynamics at the time of plate formation and, in particular, for distinguishing between two end-member ridge processes (Blackman et al., 1996): (1) passive upwelling and (2) buoyancy-driven upwelling. Observations of $V_{SV} > V_{SH}$ in the upper ~100 km of the mantle beneath the Reykjanes Ridge have been used to infer hot spot-induced buoyant upwelling (Gaherty, 2001), although alternative interpretation in terms of 3-D flow have been proposed (Delorey et al., 2007). This interpretation is consistent with numerical models of such buoyancy-driven upwelling at slow-spreading ridges, which predict primarily vertical off-axis fabrics associated with the downgoing limb of cooler mantle material, extending from the Moho down to 40–50 km depth (Blackman et al., 1996; Blackman & Kendall, 2002a). Conversely, numerical flow models of passive upwelling at fast-spreading ridges produce primarily horizontal lithospheric fabrics that are oriented in the direction of spreading and increase in strength with depth in the lithosphere (Blackman et al., 1996, 2017; Blackman & Kendall, 2002a, 2002b).

Radial and azimuthal anisotropy observed at NoMelt are consistent with features of the passive upwelling model. We observe $\xi > 1$ as well as G and E directions parallel to FSD and FSD+45°, respectively, which are all consistent with horizontal lithospheric fabric that formed due to corner flow at the ridge. Furthermore, our observations of a positive gradient in G from the Moho to ~30 km depth is consistent with numerical flow models of passive spreading that predict a positive gradient in LPO strength within the upper 20–80 km of the mantle (Blackman et al., 1996, 2017; Blackman & Kendall, 2002a). The depth-dependent LPO strength predicted by flow models is a result of the positive temperature gradient, which reduces viscosities leading to higher strain and enhanced fabric alignment with depth.

Although the strength of G varies within in the lithosphere, Ψ_G remains parallel to fossil spreading down to 80–90 km depth. One interpretation is that this depth marks the dehydration boundary above which volatiles were extracted to form the dry, rigid lithosphere locking in the spreading-parallel fabric. Below 80–90 km depth, we observe the transition from the seismically fast lid to the LVZ (Figure 11a), a minimum in G, and a rotation in Ψ_G away from fossil spreading. Together, these observations are consistent with the transition from lithosphere to the weaker asthenosphere with a rotated fabric that underlies the dehydration boundary. This interpretation agrees with the high electrical resistivities ($> 10^3$ Ωm) observed in the upper ~80 km beneath NoMelt attributed to dehydrated lithosphere (Sarafian et al., 2015).

In contrast to our observations of FSD-parallel fabric throughout the lithosphere, departures in the fast direction away from fossil spreading have been observed at the East Pacific Rise (Toomey et al., 2007), Juan de Fuca ridge (Vanderbeek & Toomey, 2017), and in the south (Takeo et al., 2016) and NW Pacific (Shintaku et al., 2014; Takeo et al., 2018). Rotations ranging from 9° to 70° have been observed at depths of 4–60 km beneath the Moho. These rotations have been attributed to spreading-oblique flow at the base of the plate that reorganizes and overprints the spreading-parallel signal before being incorporated into the LPO fabric as the lithosphere cools (e.g., Toomey et al., 2007). According to plate reconstructions by Seton et al. (2012), Pacific plate motion 60–80 Ma was to the NW with spreading oriented approximately E-W at the ridge. Therefore, an ancient plate motion signal would manifest as a clockwise rotation in lithospheric Ψ_G (and Ψ_E) at NoMelt, similar to that observed by Takeo et al. (2016) at TIARES. Although the ancient apparent plate motions were similar in the two regions, the half-spreading rate is relatively fast (4-5 cm/year) at NoMelt and slow (2–3 cm/year) at TIARES (Müller et al., 2008; Takeo et al., 2016). The difference in fast direction between these regions may reflect that lithosphere fabric records the FSD if spreading rate is large relative to absolute plate velocity, while fabric is dominated by APM if spreading rate is slow. This suggests spreading rate may play an important role in determining not only the strength of anisotropy in the lithosphere (e.g., Gaherty et al., 2004; Song & Kim, 2011) but also its direction relative to spreading. The LPO fabric inferred

from the strength and direction of G and E observed in the lithosphere at NoMelt will help improve future models of MOR dynamics.

7.4. Radial Anisotropy in the Crust

Strong radial anisotropy is required in the lower crust with V_{SH}4-5% faster than V_{SV}, suggesting layered horizontal crustal fabrics and/or shear. Radial anisotropy in the crust has not been observed in previous surface-wave studies, perhaps due to the lack of high-frequency data with strong sensitivity to the crust; however, it is required by our data set in order to simultaneously fit the high-frequency Rayleigh- and Love-wave dispersion to within the error bounds of the data (Figures 8e–8g and S3–S6). Forcing the crust to be isotropic produces Rayleigh-wave velocities that are overpredicted at the shorter periods and underpredicted at longer periods, resulting in large overall data misfit ($\chi^2 \approx 17$). Furthermore, allowing for a more complex mantle structure with additional layers of anisotropy does not significantly change its strength in the crust, suggesting that it is not an artifact of underparameterization but is truly a robust feature of our model.

Anisotropy with $V_{SH} > V_{SV}$ may be consistent with crustal accretion processes including the "gabbro glacier" model (e.g., Morgan & Chen, 1993) where accretion occurs through ductile flow from a midcrustal magma lens and the "sheeted sill" model (e.g., Boudier et al., 1996) where sills are injected throughout the crust at the ridge, if these processes produce significant vertical variations in either isotropic velocities or anisotropic fabric. Horizontal crustal fabrics have been observed at the Samail ophiolite, where plagioclase in the lower crust is characterized by a strong foliation ([010] axis vertical) and weak lineation ([100] axis girdle in horizontal plane) indicating horizontal strain via compaction (VanTongeren et al., 2015). A fabric of this character should produce radial anisotropy with $V_{SH} > V_{SV}$ and weak to no azimuthal anisotropy, similar to what we observe.

Further evidence for quasi-horizontal fabrics in the lower crust comes from lower crustal reflectors observed in the northwest Pacific dipping toward the paleo-ridge axis at 20–25° (Kodaira et al., 2014; Reston et al., 1999) and south of the Alaska Peninsula with dips of 10–30° (Bécel et al., 2015). These dipping reflectors typically extend from the Moho to the top of layer 3 and are thought to originate from shear zones in the ductile lower crust during accretion, requiring differential motion between the crust and mantle (Bécel et al., 2015; Kodaira et al., 2014). In both scenarios, the accretion and/or shearing process produce short-wavelength velocity variations that are large enough to reflect high-frequency seismic energy and produce apparent surface-wave radial anisotropy through Backus averaging (Backus, 1962). Our observation of $\xi \sim 1.1$ suggests root-mean-square shear-velocity variations of approximately 16% (Gee & Jordan, 1988), consistent with intracrustal reflectors that are comparable to the brightness of the Moho (Bécel et al., 2015). Our results are inconsistent with vertical diking and/or vertical cracks, which should produce fast V_{SV} relative to V_{SH} ($\xi < 1$) as well as crack-parallel (ridge-parallel) Rayleigh-wave fast directions (Hudson, 1981; Thomsen, 1995), neither of which we observe.

8. Conclusion

We use high-frequency ambient-noise Rayleigh and Love waves (5–7.5 s) in addition to previously analyzed 15- to 150-s Rayleigh waves recorded on the NoMelt array to provide high-resolution, in situ constraints on seismic anisotropy parameters ξ, G, and E for the upper ~30 km of the mantle (Figure 12). We measure the full azimuthal variability of surface waves including Rayleigh-2θ behavior, and for the first time, Love-2θ and Love-4θ variability. The data require radial anisotropy with $\xi > 1$ in the uppermost Pacific lithosphere and crust, in contrast to recent global models that show $\xi < 1$ throughout the lithosphere. G is stronger in the lithosphere than the asthenosphere, reaching a peak of ~6% at ~30 km depth and has a direction parallel to the FSD down to 80–90 km depth, perhaps marking the depth to the dehydration boundary and LAB. We provide the first high-resolution estimates of E parallel to FSD+45° with a strength of 2–2.5% down to 35 km depth. Our in situ surface wave constraints on ξ, G, and E agree in magnitude and direction with oceanic petrofabric observations, suggesting extremely coherent LPO fabric within the NoMelt footprint and bridging the gap between surface-wave and outcrop length scales. Furthermore, strong azimuthal anisotropy and relatively weak radial anisotropy in the lithosphere at NoMelt indicate either E-type LPO fabric or A-type fabric with its fast axis rotated slightly out of the horizontal plane. Observations of G and E azimuths, the increase in strength of G with depth, and $\xi > 1$ in the upper ~30 km of the mantle are consistent with numerical flow model predictions of LPO fabric produced by corner flow at the passively upwelling ridge. Strong radial anisotropy in the lower crust with $\xi > 1$ suggests horizontal layering consistent with either the gabbro glacier and sheeted sill models of crustal accretion.

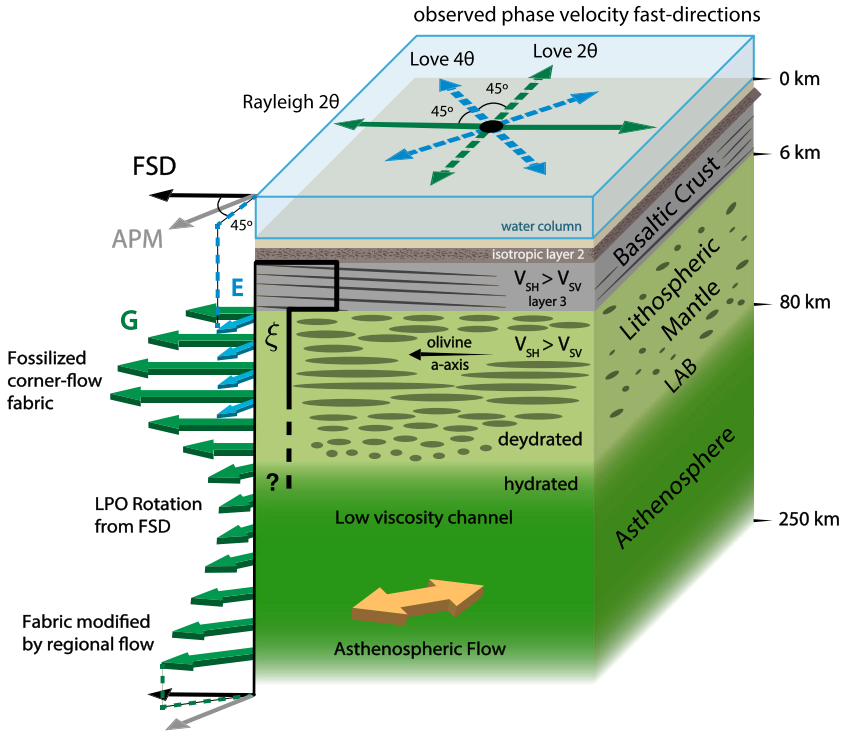

Figure 12. Interpretation of the crust and upper mantle beneath NoMelt. Observed Rayleigh-2θ and Love-2θ and -4θ variations in phase velocity are shown with fast directions parallel to FSD, FSD+90°, and FSD+45°, respectively. Olivine a-axes are subhorizontal with LPO strength increasing from the Moho to ~30 km depth, consistent with numerical flow models of passive upwelling. *G* is parallel to fossil spreading from the Moho down to 80–90 km depth where it rotates to a direction intermediate to FSD and APM, perhaps marking the depth at which dehydration occurred at the ridge, thus locking in lithosphere LPO and forming the LAB. The rotation and minimum in *G* below 80 km suggests a low viscosity decoupling zone beneath the plate. Deeper in the asthenosphere, *G* reflects the asthenospheric flow pattern, which is not parallel to plate motion, suggesting deformation associated with regional flow dominates. Strong horizontal fabric ($V_{SH} > V_{SV}$) is observed in the lower crust (layer 3), consistent with both the "gabbro glacier" and "sheeted sill" models of crustal accretion involving horizontal layering and/or shearing. FSD = fossil-spreading direction; LPO = lattice-preferred orientation; APM = absolute plate motion; LAB = lithosphere-asthenosphere boundary.

Appendix A: Seismic Anisotropy Parameterization

The full anisotropic complexity of surface waves traveling through a weakly anisotropic medium can be described by 13 independent elastic parameters, composing the elastic stiffness tensor C_{ij}. In practice, this elastic tensor can be divided into two parts:

$$C_{ij} = C_{ij}^{TI} + \delta C_{ij}\,, \tag{A1}$$

where C_{ij}^{TI} consists of five independent parameters describing the transversely isotropic part that satisfies the azimuthally averaged Rayleigh- and Love-wave phase velocities, and δC_{ij} consists of eight independent parameters describing the azimuthally anisotropic part that captures the 2θ and 4θ azimuthal variations of surface waves. In this study, we constrain the full elastic tensor by solving separately for C_{ij}^{TI} and δC_{ij}.

The azimuthally averaged transversely isotropic part, C_{ij}^{TI}, is parameterized by horizontally propagating vertically and horizontally polarized *S* wave speeds (V_{SV}, V_{SH}); vertically and horizontally propagating *P* wave speeds (V_{PV}, V_{PH}); the parameter η, which influences waves traveling at angles intermediate to the symmetry axis but lacks a clear physical meaning (Kawakatsu, 2016a, 2016b); and density ρ (or equivalently, Love's parameters *A*, *C*, *L*, *N*, and *F*). These moduli can be written in terms of the full elastic tensor in equation (A1) (Montagner & Nataf, 1986):

$$A = \rho V_{PH}^2 = \frac{3}{8}(C_{11} + C_{22}) + \frac{1}{4}C_{12} + \frac{1}{2}C_{66}\,, \tag{A2}$$

$$C = \rho V_{PV}^2 = C_{33}, \tag{A3}$$

$$L = \rho V_{SV}^2 = \frac{1}{2}(C_{55} + C_{44}), \tag{A4}$$

$$N = \rho V_{SH}^2 = \frac{1}{8}(C_{11} + C_{22}) - \frac{1}{4}C_{12} + \frac{1}{2}C_{66}, \tag{A5}$$

$$F = \rho\eta(V_{PH}^2 - 2V_{SV}^2) = \frac{1}{2}(C_{13} + C_{23}), \tag{A6}$$

$$\xi = \left(\frac{V_{SH}}{V_{SV}}\right)^2 = \frac{N}{L}, \tag{A7}$$

where radial anisotropy, ξ, is a proxy for vertical ($\xi < 1$) or horizontal ($\xi > 1$) flow in the mantle when produced by the LPO of olivine. The transversely isotropic earth defined in this way is equivalent to a hexagonal crystal with a vertical symmetry axis and sufficiently describes average global body- and surface-wave data sets (Anderson & Dziewonski, 1982; Dziewonski & Anderson, 1981).

If olivine LPO is coherent at the local or regional scale, A, L, N, and F will also vary with propagation azimuth, resulting in a lower symmetry system that exhibits azimuthal anisotropy (Montagner, 2002). The azimuthal variation of each elastic moduli around its average value, δC_{ij}, is described by a magnitude (G, B, H, and E) and corresponding direction (Ψ_G, Ψ_B, Ψ_H, and Ψ_E) of anisotropy:

2θ :

$$G = \delta L = \sqrt{G_c^2 + G_s^2}, \qquad \Psi_G = \frac{1}{2}\arctan\left(\frac{G_s}{G_c}\right); \tag{A8}$$

$$B = \delta A = \sqrt{B_c^2 + B_s^2}, \qquad \Psi_B = \frac{1}{2}\arctan\left(\frac{B_s}{B_c}\right); \tag{A9}$$

$$H = \delta F = \sqrt{H_c^2 + H_s^2}, \qquad \Psi_H = \frac{1}{2}\arctan\left(\frac{H_s}{H_c}\right); \tag{A10}$$

4θ :

$$E = \delta N = \sqrt{E_c^2 + E_s^2}, \qquad \Psi_E = \frac{1}{4}\arctan\left(\frac{-E_s}{-E_c}\right); \tag{A11}$$

$$G_c = \frac{1}{2}(C_{55} - C_{44}), \tag{A12}$$

$$G_s = C_{54}, \tag{A13}$$

$$B_c = \frac{1}{2}(C_{11} - C_{22}), \tag{A14}$$

$$B_s = C_{16} + C_{26}, \tag{A15}$$

$$H_c = \frac{1}{2}(C_{13} - C_{23}), \tag{A16}$$

$$H_s = C_{36}, \tag{A17}$$

$$E_c = \frac{1}{8}(C_{11} + C_{22}) - \frac{1}{4}C_{12} - \frac{1}{2}C_{66}, \tag{A18}$$

$$E_s = \frac{1}{2}(C_{16} - C_{26}), \tag{A19}$$

In this case, the direction and strength of anisotropy depend on the bulk orientation and degree of organization of olivine [100] axes within the horizontal plane. The azimuthal variation of body-wave velocities are a direct function of these elastic parameters (Crampin, 1977):

$$\rho V_{qP}(\theta)^2 = A + B_c \cos(2\theta) + B_s \sin(2\theta) + E_c \cos(4\theta) + E_s \sin(4\theta), \tag{A20}$$

$$\rho V_{qSV}(\theta)^2 = L + G_c \cos(2\theta) + G_s \sin(2\theta), \tag{A21}$$

$$\rho V_{qSH}(\theta)^2 = N - E_c \cos(4\theta) - E_s \sin(4\theta), \tag{A22}$$

where θ is the propagation azimuth and V_{qP}, V_{qSV}, and V_{qSH} are the velocities of quasi compressional- and shear-waves propagating along the horizontal plane. The azimuthal anisotropy of surface waves is more complex; Rayleigh waves propagate with a 2θ azimuthal dependence controlled by G, B, and H with a fast direction parallel to the horizontal [100] axis of olivine, and Love waves exhibit both a 2θ and 4θ azimuthal dependence controlled by G and E, respectively (Montagner & Nataf, 1986). Love-wave azimuthal anisotropy has remained poorly constrained owing to a lack of azimuthal coverage and the high noise levels typically observed on the horizontal components.

The complete C_{ij} can be constructed from the transversely isotropic and azimuthal terms by rearranging equations ((A2)–(A6); (A12)–(A19)):

$$C_{ij} = \begin{pmatrix} A + B_c + E_c & A - 2N - E_c & F + H_c & 0 & 0 & \frac{1}{2}B_s + E_s \\ \cdot & A - B_c + E_c & F - H_c & 0 & 0 & \frac{1}{2}B_s - E_s \\ \cdot & \cdot & C & 0 & 0 & H_s \\ \cdot & \cdot & \cdot & L - G_c & G_s & 0 \\ \cdot & \cdot & \cdot & \cdot & L + G_c & 0 \\ \cdot & \cdot & \cdot & \cdot & \cdot & N - E_c \end{pmatrix} \tag{A23}$$

Of the 13 parameters, only 6 (primarily shear) parameters are well resolved by Rayleigh (L or V_{SV}; $G_{c,s}$) and Love waves (N or V_{SH}; $E_{c,s}$) and therefore, symmetry relations and a priori information must be used to constrain the remaining 7 parameters. In this study, we apply such constraints to account for all 13 elastic parameters, focusing our interpretations primarily on the most well-resolved ones: ξ, G, Ψ_G, E, and Ψ_E.

Acknowledgments
We thank the captain, crew, and engineers of the R/V *Marcus G. Langseth* for making the data collection possible. OBS were provided by Scripps Institution of Oceanography via the Ocean Bottom Seismograph Instrument Pool (http://www.obsip.org), which is funded by the National Science Foundation. All waveform data used in this study are archived at the IRIS Data Management Center (http://www.iris.edu) with network code ZA for 2011–2013, and all OBS orientations are included in Table S1. The 1-D transversely isotropic and azimuthally anisotropic models and their uncertainties from this study can be found in the supporting information. This work was supported by NSF grants OCE-0928270 and OCE-1538229 (J. B. Gaherty), EAR-1361487 (G. Hirth), and OCE-0938663 (D. Lizarralde, J. A. Collins, and R. L. Evans), and an NSF Graduate Research Fellowship DGE-16-44869 to J. B. Russell. The authors thank the editor as well as reviewers Donald Forsyth, Hitoshi Kawakatsu, and Thorsten Becker for their constructive comments, which significantly improved this manuscript. J. B. Russell thanks Natalie J. Accardo for kindly sharing codes and expertise that contributed greatly to the analysis.

References

Aki, K. (1957). Space and time spectra of stationary stochastic waves, with special reference to microtremors. *Bulletin of the Earthquake Research Institute*, *35*(3), 415–456.

Anderson, D. L. (1961). Elastic wave propagation in layered anisotropic media. *Journal of Geophysical Research*, *66*(9), 2953–2963.

Anderson, D. L., & Dziewonski, A. M. (1982). Upper mantle anisotropy: Evidence from free oscillations. *Geophysical Journal of the Royal Astronomical Society*, *69*, 383–404.

Argus, D. F., & Gordon, R. G. (1991). No-net-rotation model of current plate velocities incorporating plate motion model NUVEL-1. *Geophysical Research Letters*, *18*, 2039–2042.

Backus, G. E. (1962). Long-wave elastic anisotropy produced by horizontal layering. *Journal of Geophysical Research*, *67*(11), 4427–4440.

Bécel, A., Shillington, D. J., Nedimovi, M. R., Webb, S. C., & Kuehn, H. (2015). Origin of dipping structures in fast-spreading oceanic lower crust offshore Alaska imaged by multichannel seismic data. *Earth and Planetary Science Letters*, *424*, 26–37. https://doi.org/10.1016/j.epsl.2015.05.016

Becker, T. W., Conrad, C. P., Schaeffer, A. J., & Lebedev, S. (2014). Origin of azimuthal seismic anisotropy in oceanic plates and mantle. *Earth and Planetary Science Letters*, *401*, 236–250. https://doi.org/10.1016/j.epsl.2014.06.014

Beghein, C., Yuan, K., Schmerr, N., & Xing, Z. (2014). Changes in seismic anisotropy shed light on the nature of the Gutenberg discontinuity. *Science (New York, N.Y.)*, *343*(6176), 1237–40. Retrieved from http://www.ncbi.nlm.nih.gov/pubmed/24578529 https://doi.org/10.1126/science.1246724

Bensen, G. D., Ritzwoller, M. H., Barmin, M. P., Levshin, A. L., Lin, F., Moschetti, M. P., & Yang, Y. (2007). Processing seismic ambient noise data to obtain reliable broad-band surface wave dispersion measurements. *Geophysical Journal International*, *169*(3), 1239–1260. https://doi.org/10.1111/j.1365-246x.2007.03374.x

Blackman, D. K., Boyce, D. E., Castelnau, O., Dawson, P. R., & Laske, G. (2017). Effects of crystal preferred orientation on upper-mantle flow near plate boundaries: Rheologic feedbacks and seismic anisotropy. *Geophysical Journal International*, *210*, 1481–1493. https://doi.org/10.1093/gji/ggx251

Blackman, D. K., & Kendall, J. M. (2002a). Seismic anisotropy in the upper mantle 2. Predictions for current plate boundary flow models. *Geochemistry, Geophysics, Geosystems*, *3*(9), 8602. https://doi.org/10.1029/2001GC000247

Blackman, D. K., & Kendall, J. M. (2002b). Seismic anisotropy of the upper mantle 1. Factors that affect mineral texture and effective elastic properties. *Geochemistry, Geophysics, Geosystems*, *3*(9), 8601. https://doi.org/10.1029/2001GC000248

Blackman, D. K., Kendall, J., Paul, R. D., Wenk, H., Boyce, D., & Morgan, J. P. (1996). Teleseismic imaging of subaxial flow at mid-ocean ridges: Traveltime effects of anisotropic mineral texture in the mantle. *Geophysical Journal International*, *127*, 415–426.

Boudier, F., Nicolas, A., & Ildefonse, B. (1996). Magma chambers in the Oman ophiolite: Fed from the top and the bottom. *Earth and Planetary Science Letters*, *144*(96), 239–250.

Brocher, T. M. (2005). Empirical relations between elastic wavespeeds and density in the Earth's crust. *Bulletin of the Seismological Society of America*, *95*(6), 2081–2092. https://doi.org/10.1785/0120050077

Burgos, G., Montagner, J. P., Beucler, E., Capdeville, Y., Mocquet, A., & Drilleau, M. (2014). Oceanic lithosphere-asthenosphere boundary from surface wave dispersion data. *Journal of Geophysical Research: Solid Earth*, *119*, 1079–1093. https://doi.org/10.1002/2013JB010528

Cox, H. (1973). Spatial correlation in arbitrary noise fields with application to ambient sea noise. *The Journal of the Acoustical Society of America*, *54*, 1289–1301. https://doi.org/10.1121/1.1914426

Crampin, S. (1977). A review of the effects of anisotropic layering. *Geophysical Journal of the Royal Astronomical Society*, *49*, 9–27.

Crampin, S. (1981). A review of wave motion in anisotropic and cracked elastic-media. *Wave Motion*, *3*, 343–391. https://doi.org/10.1016/0165-2125(81)90026-3

Davison, A., Hinkley, D., & Schechtman, E. (1986). Efficient bootstrap simulation. *Biometrika*, *73*(3), 555–566.

Debayle, E., & Ricard, Y. (2013). Seismic observations of large-scale deformation at the bottom of fast-moving plates. *Earth and Planetary Science Letters*, *376*, 165–177. https://doi.org/10.1016/j.epsl.2013.06.025

Delorey, A. A., Dunn, R. A., & Gaherty, J. B. (2007). Surface wave tomography of the upper mantle beneath the Reykjanes Ridge with implications for ridge–hot spot interaction. *Journal of Geophysical Research*, *112*, B08313. https://doi.org/10.1029/2006JB004785

Doran, A. K., & Laske, G. (2017). Ocean-bottom seismometer instrument orientations via automated Rayleigh-wave arrival-angle measurements. *Bulletin of the Seismological Society of America*, *107*(2), 691–708. https://doi.org/10.1785/0120160165

Dziewonski, A. M., & Anderson, D. L. (1981). Preliminary reference Earth model * Adam M. *Physics of the Earth and Planetary Interiors*, *25*, 297–356.

Eddy, C. L., Ekström, G., Nettles, M., & Gaherty, J. B. (2018). Age dependence and anisotropy of surface-wave phase velocities in the Pacific. *Geophysical Journal International*, *216*, 640–658. https://doi.org/10.1093/gji/ggy438

Ekström, G., & Dziewonski, A. M. (1998). The unique anisotropy of the Pacific upper mantle. *Nature*, *394*(6689), 168–172. Retrieved from http://www.nature.com/doifinder/10.1038/28148, https://doi.org/10.1038/28148

Forsyth, D. W. (1975). The early structural evolution and anisotropy of the oceanic upper mantle. *Geophysical Journal of the Royal Astronomical Society*, *43*(1), 103–162.

Forsyth, D. W., Webb, S. C., Dorman, L. M., & Shen, Y. (1998). East Pacific Rise phase velocities of Rayleigh waves in the MELT Experiment on the East Pacific Rise. *Science*, *280*, 1235–1238. https://doi.org/10.1126/science.280.5367.1235

French, S. W., & Romanowicz, B. A. (2014). Whole-mantle radially anisotropic shear velocity structure from spectral-element waveform-tomography. *Geophysical Journal International*, *199*, 1303–1327. https://doi.org/10.1093/gji/ggu334

Gaherty, J. B. (2001). Seismic evidence for hotspot-induced buoyant flow beneath the Reykjanes Ridge. *Science*, *293*, 1645–1647.

Gaherty, J. B., Jordan, T. H., & Gee, L. S. (1996). Seismic structure of the upper mantle in a central Pacific corridor. *Journal of Geophysical Research*, *101*, 22,291–22,309.

Gaherty, J. B., Lizarralde, D., Collins, J. A., Hirth, G., & Kim, S. (2004). Mantle deformation during slow seafloor spreading constrained by observations of seismic anisotropy in the western Atlantic. *Earth and Planetary Science Letters*, *228*, 255–265. https://doi.org/10.1016/j.epsl.2004.10.026

Gee, L. S., & Jordan, T. H. (1988). Polarization anisotropy and finescale structure of the Eurasian upper mantle. *Geophysical Research Letters*, *15*(8), 824–827. https://doi.org/10.1029/GL015i008p00824

Hess, H. (1964). Seismic anisotropy of the uppermost mantle under oceans. *Nature*, *203*, 629–631.

Holtzman, B. K., & Kendall, J. M. (2010). Organized melt, seismic anisotropy, and plate boundary lubrication. *Geochemistry, Geophysics, Geosystems*, *11*, Q0AB06. https://doi.org/10.1029/2010GC003296

Hudson, A. (1981). Material containing cracks. *Geophysical Journal of the Royal Astronomical Society*, *64*, 133–150.

Hung, W. l., Lee, E. S., & Chuang, S. c. (2011). Balanced bootstrap resampling method for neural model selection. *Computers and Mathematics with Applications*, *62*(12), 4576–4581. https://doi.org/10.1016/j.camwa.2011.10.039

Ismail, W. B., & Mainprice, D. (1998). An olivine fabric database: An overview of upper mantle fabrics and seismic anisotropy. *Tectonophysics*, *296*, 145–157. https://doi.org/10.1016/S0040-1951(98)00141-3

Jung, H., & Karato, S. i. (2001). Water-induced fabric transitions in olivine. *Science*, *293*, 1460–1464.

Jung, H., Katayama, I., Jiang, Z., Hiraga, T., & Karato, S. (2006). Effect of water and stress on the lattice-preferred orientation of olivine. *Tectonophysics*, *421*, 1–22. https://doi.org/10.1016/j.tecto.2006.02.011

Kaminski, É., & Ribe, N. M. (2001). A kinematic model for recrystallization and texture development in olivine polycrystals. *Earth and Planetary Science Letters*, *189*, 253–267.

Kaminski, É., & Ribe, N. M. (2002). Timescales for the evolution of seismic anisotropy in mantle flow. *Geochemistry, Geophysics, Geosystems*, *3*(8), 1051. https://doi.org/10.1029/2001GC000222

Karato, S. i., Jung, H., Katayama, I., & Skemer, P. (2008). Geodynamic significance of seismic anisotropy of the upper mantle: New insights from laboratory studies. *Annual Review Earth and Planetary Sciences*, *36*, 59–95. https://doi.org/10.1146/annurev.earth.36.031207.124120

Kawakatsu, H. (2016a). A new fifth parameter for transverse isotropy. *Geophysical Journal International*, *204*, 682–685. https://doi.org/10.1093/gji/ggv479

Kawakatsu, H. (2016b). A new fifth parameter for transverse isotropy II: Partial derivatives. *Geophysical Journal International*, *206*, 360–367. https://doi.org/10.1093/gji/ggw152

Kawakatsu, H., & Utada, H. (2017). Seismic and electrical signatures of the lithosphere asthenosphere system of the normal oceanic mantle. *Annual Review Earth and Planetary Sciences*, *45*, 139–167.

Keen, C. E., & Barrett, D. L. (1971). A measurement of seismic anistropy in the northeast Pacific. *Canadian Journal of Earth Sciences*, *8*, 1056–1064.

Kennett, B. L. N., & Furumura, T. (2013). High-frequency Po/So guided waves in the oceanic lithosphere: I—Long-distance propagation. *Geophysical Journal International*, *195*, 1862–1877. https://doi.org/10.1093/gji/ggt344

Kennett, B. L. N., Furumura, T., & Zhao, Y. (2014). High-frequency Po/So guided waves in the oceanic lithosphere: II—Heterogeneity and attenuation. *Geophysical Journal International*, *199*, 614–630. https://doi.org/10.1093/gji/ggu286

Kodaira, S., Fujie, G., Yamashita, M., Sato, T., Takahashi, T., & Takahashi, N. (2014). Seismological evidence of mantle flow driving plate motions at a palaeo-spreading centre. *Nature Geoscience*, *7*(5), 371–375. https://doi.org/10.1038/ngeo2121

Kustowski, B., Ekstro, G., & Dziewonski, A. M. (2008). Anisotropic shear-wave velocity structure of the Earth's mantle: A global model. *Journal of Geophysical Research*, *113*, B06306. https://doi.org/10.1029/2007JB005169

Laske, G., Masters, G., Ma, Z., & Pasyanos, M. (2013). Update on CRUST1.0 - A 1-degree global model of Earth's crust. In *EGU General Assembly Conference Abstracts* (Vol. 15, EGU2013-2658). Retrieved from http://adsabs.harvard.edu/abs/2013EGUGA..15.2658L

Lin, P. Y. P., Gaherty, J. B., Jin, G., Collins, J. A., Lizarralde, D., Evans, R. L., & Hirth, G. (2016). High-resolution seismic constraints on flow dynamics in the oceanic asthenosphere. *Nature*, *535*(7613), 1–9. https://doi.org/10.1038/nature18012

Lizarralde, D., Gaherty, J. B., Collins, J. A., Hirth, G., & Evans, R. L. (2012). Structure of Pacific-plate upper mantle from active-source seismic measurements of the NoMelt experiment. In *Abstract T33G-2732 presented at 2012 Fall Meeting, AGU, San Francisco, Calif., 3-7 Dec.*

Long, M. D., & Silver, P. G. (2009). Shear wave splitting and mantle anisotropy: Measurements, interpretations, and new directions. *Surveys in Geophysics*, *30*, 407–461. https://doi.org/10.1007/s10712-009-9075-1

Mainprice, D. (2015). Seismic anisotropy of the deep earth from a mineral and rock physics perspective. In G. Schubert (Ed.), *Treatise on Geophysics* (2nd ed., Vol. 2, pp. 487–538). Oxford: Elsevier. Retrieevd from http://www.sciencedirect.com/science/article/pii/B9780444538024000440

Mark, H., Lizarralde, D., Collins, J. A., Miller, N. C., Hirth, G., Gaherty, J. B., & Evans, R. L. (2017). Seismic anisotropy of 70 Ma Pacific-plate upper mantle. In *Abstract DI51D-05 presented at 2017 Fall Meeting, AGU, New Orleans, LA, 11-15 Dec.*

Menke, W. (2012). Geophysical data analysis: Discrete inverse theory. Retrieved from http://linkinghub.elsevier.com/retrieve/pii/B9780123971609000199, https://doi.org/10.1016/B978-0-12-397160-9.00019-9

Menke, W., & Jin, G. (2015). Waveform fitting of cross spectra to determine phase velocity using Aki's formula. *Bulletin of the Seismological Society of America*, *105*(3), 1619–1627. Retrieved from http://www.bssaonline.org/content/105/3/1619.abstract, https://doi.org/10.1785/0120140245

Montagner, J. P. (2002). Upper mantle low anisotropy channels below the Pacifc plate. *Earth and Planetary Science Letters*, *202*, 263–274.

Montagner, J. P., & Anderson, D. L. (1989). Petrological constraints on seismic anisotropy. *Physics of the Earth and Planetary Interiors*, *54*, 82–105.

Montagner, J. P., & Nataf, H. C. (1986). A simple method for inverting the azimuthal anisotropy of surface waves. *Journal of Geophysical Research*, *91*, 511–520.

Montagner, J. P., & Tanimoto, T. (1990). Global anisotropy in the upper mantle inferred from the regionalization of phase velocities. *Journal of Geophysical Research*, *95*(B4), 4797–4819.

Montagner, J. P., & Tanimoto, T. (1991). Global upper mantle tomography of seismic velocities and anisotropies. *Journal of Geophysical Research*, *96*(9), 20,337–20,351.

Morgan, J. P., & Chen, Y. J. (1993). The genesis of oceanic crust: Magma injection, hydrothermal circulation, and crustal flow. *Journal of Geophysical Research*, *98*, 6283–6297.

Morris, G. B., Raitt, R. W., & Shor, G. G. (1969). Velocity anisotropy and delay-time maps of the mantle near Hawaii. *Journal of Geophysical Research*, *74*(17), 4300–4316. https://doi.org/10.1029/JB074i017p04300

Moulik, P., & Ekström, G. (2014). An anisotropic shear velocity model of the Earth's mantle using normal modes, body waves, surface waves and long-period waveforms. *Geophysical Journal International*, *199*(3), 1713–1738. https://doi.org/10.1093/gji/ggu356

Müller, R. D., Sdrolias, M., Gaina, C., & Roest, R. W. (2008). Age, spreading rates, and spreading asymmetry of the world's ocean crust. *Geochemistry, Geophysics, Geosystems*, *9*, Q04006. https://doi.org/10.1029/2007GC001743

Nettles, M., & Dziewoński, A. M. (2008). Radially anisotropic shear velocity structure of the upper mantle globally and beneath North America. *Journal of Geophysical Research*, *113*, B02303. Retrieved from http://doi.wiley.com/10.1029/2006JB004819, https://doi.org/10.1029/2006JB0048191

Nicolas, A., & Christensen, N. I. (1987). Formation of anisotropy in upper mantle peridotites—A Review. In K. Fuchs & C. Froidevaux (Eds.), *Composition, Structure, and Dynamics of Lithosphere Asthenosphere system* (Vol. 16, pp. 111–123). Washington, DC: American Geophysical Union.

Nishida, K., Kawakatsu, H., & Obara, K. (2008). Three-dimensional crustal S wave velocity structure in Japan using microseismic data recorded by Hi-net tiltmeters. *Journal of Geophysical Research*, *113*, B10302. https://doi.org/10.1029/2007JB005395

Nishimura, C. E., & Forsyth, D. W. (1989). The anisotropic structure of the upper mantle in the Pacific Ocean. *Geophysical Journal of the Royal Astronomical Society*, *96*(2), 203–229.

Panning, M., & Romanowicz, B. (2006). A three-dimensional radially anisotropic model of shear velocity in the whole mantle. *Geophysical Journal International*, *167*, 361–379. https://doi.org/10.1111/j.1365-246x.2006.03100.x

Peselnick, L., & Nicolas, A. (1978). Seismic anisotropy in an ophiolite peridotite: Application to oceanic upper mantle. *Journal of Geophysical Research*, *83*(B3), 1227–1235.

Raitt, R. W., Shor, G. G., Francis, T. J. G., & Morris, G. B. (1969). Anisotropy of the Pacific upper mantle. *Journal of Geophysical Research*, *74*(12), 3095–3109.

Reston, T. J., Ranero, C. R., & Belykh, I. (1999). The structure of Cretaceous oceanic crust of the NW Pacific: Constraints on processes at fast spreading ridges. *Journal of Geophysical Research*, *104*, 629–644.

Ribe, N. M. (1989). A continuum theory for lattice preferred orientation. *Geophysical Journal International*, *97*, 199–207.

Ruan, Y., Forsyth, D. W., & Bell, S. W. (2014). Marine sediment shear velocity structure from the ratio of displacement to pressure of Rayleigh waves at seafloor. *Journal of Geophysical Research : Solid Earth*, *119*, 6357–6371. https://doi.org/10.1002/2014JB011162

Rychert, C. A., & Harmon, N. (2017). Constraints on the anisotropic contributions to velocity discontinuities at ~60 km depth beneath the Pacific. *Geochemistry, Geophysics, Geosystems*, *18*, 2855–2871. https://doi.org/10.1002/2017GC006850

Sarafian, E., Evans, R. L., Collins, J. A., Elsenbeck, J., Gaetani, G. A., Gaherty, J. B., & Lizarralde, D. (2015). The electrical structure of the central Pacific upper mantle constrained by the NoMelt experiment. *Geochemistry, Geophysics, Geosystems*, *16*, 1115–1132. https://doi.org/10.1002/2014GC005709

Savage, M. K. (1999). Seismic anisotropy and mantle deformation: What have we learned from shear wave splitting? *Reviews of Geophysics*, *37*(98), 65–106.
Schaeffer, A. J., Lebedev, S., & Becker, T. W. (2016). Azimuthal seismic anisotropy in the Earth's uppermantle and the thickness of tectonic plates. *Geophysical Journal International*, *207*(2), 901–933. https://doi.org/10.1093/gji/ggw309
Seton, M., Müller, R. D., Zahirovic, S., Gaina, C., Torsvik, T., Shephard, G., & Chandler, M. (2012). Earth-science reviews global continental and ocean basin reconstructions since 200 Ma. *Earth Science Reviews*, *113*, 212–270. https://doi.org/10.1016/j.earscirev.2012.03.002
Shintaku, N., Forsyth, D. W., Hajewski, C., & Weeraratne, D. S. (2014). Pn anisotropy in Mesozoic western Pacific lithosphere. *Journal of Geophysical Research: Solid Earth*, *119*, 3050–3063. https://doi.org/10.1002/2013JB010534
Shito, A., Suetsugu, D., & Furumura, T. (2015). Evolution of the oceanic lithosphere inferred from Po/So waves traveling in the Philippine Sea Plate. *Journal of Geophysical Research: Solid Earth*, *120*, 5238–5248. https://doi.org/10.1002/2014JB011814
Shito, A., Suetsugu, D., Furumura, T., Sugioka, H., & Ito, A. (2013). Small-scale heterogeneities in the oceanic lithosphere inferred from guided waves. *Geophysical Research Letters*, *40*, 1708–1712. https://doi.org/10.1002/grl.50330
Sieminski, A., Liu, Q., Trampert, J., & Tromp, J. (2007). Finite-frequency sensitivity of surface waves to anisotropy based upon adjoint methods. *Geophysical Journal International*, *168*, 1153–1174. https://doi.org/10.1111/j.1365-246x.2006.03261.x
Skemer, P., Sundberg, M., Hirth, G., & Cooper, R. (2011). Torsion experiments on coarse-grained dunite: Implications for microstructural evolution when diffusion creep is suppressed. In *Deformation mechanisms, rheology and tectonics: Microstructures, mechanics and anisotropy* (Vol. 360, pp. 211–223): Geological Society, London, Special Publications. https://doi.org/10.1144/SP360
Skemer, P., Warren, J. M., & Hirth, G. (2012). The influence of deformation history on the interpretation of seismic anisotropy. *Geochemistry, Geophysics, Geosystems*, *13*, Q03006. https://doi.org/10.1029/2011GC003988
Smith, D. B., Ritzwoller, M. H., & Shapiro, N. M. (2004). Stratification of anisotropy in the Pacific upper mantle. *Journal of Geophysical Research*, *109*, B11309. https://doi.org/10.1029/2004JB003200
Song, T. R. A., & Kim, Y. (2011). Anisotropic uppermost mantle in young subducted slab underplating Central Mexico. *Nature Geoscience*, *5*(1), 55–59. https://doi.org/10.1038/ngeo1342
Swift, S. A., Lizarralde, D., Stephen, R. A., & Hoskins, H. (1998). Velocity structure in upper ocean crust at Hole 504B from vertical seismic profiles. *Journal of Geophysical Research*, *103*, 15,361–15,376.
Takeo, A., Forsyth, D. W., Weeraratne, D. S., & Nishida, K. (2014). Estimation of azimuthal anisotropy in the NW Pacific from seismic ambient noise in seafloor records. *Geophysical Journal International*, *199*, 11–22. https://doi.org/10.1093/gji/ggu240
Takeo, A., Kawakatsu, H., Isse, T., Nishida, K., Shiobara, H., Sugioka, H., et al. (2018). In situ characterization of the lithosphere-asthenosphere system beneath NW Pacific Ocean via broadband dispersion survey with two OBS arrays. *Geochemistry, Geophysics, Geosystems*, *19*, 3529–3539. https://doi.org/10.1029/2018GC007588
Takeo, A., Kawakatsu, H., Isse, T., Nishida, K., Sugioka, H., Ito, A., & Suetsugu, D. (2016). Seismic azimuthal anisotropy in the oceanic lithosphere and asthenosphere from broadband surface wave analysis of OBS array records at 60 Ma seafloor. *Journal of Geophysical Research: Solid Earth*, *121*, 1927–1947. https://doi.org/10.1002/2015JB012429
Takeo, A., Nishida, K., Isse, T., Kawakatsu, H., Shiobara, H., & Sugioka, H. (2013). Radially anisotropic structure beneath the Shikoku Basin from broadband surface wave analysis of ocean bottom seismometer records. *Journal of Geophysical Research: Solid Earth*, *118*, 2878–2892. https://doi.org/10.1002/jgrb.50219
Tan, Y., & Helmberger, D. V. (2007). Trans-Pacific upper mantle shear velocity structure. *Journal of Geophysical Research*, *112*, B08301. https://doi.org/10.1029/2006JB004853
Thomsen, L. (1995). Elastic anisotropy due to aligned cracks in porous rock. *Geophysical Prospecting*, *43*, 805–829.
Toomey, D. R., Jousselin, D., Dunn, R. A., Wilcock, W. S. D., & Detrick, R. S. (2007). Skew of mantle upwelling beneath the East Pacific Rise governs segmentation. *Nature*, *446*, 409–414. https://doi.org/10.1038/nature05679
Trampert, J., & van Heijst, H. J. (2002). Global azimuthal anisotropy in the transition zone. *Science*, *296*, 1297–1300.
VanTongeren, J. A., Hirth, G., & Kelemen, P. B. (2015). Constraints on the accretion of the gabbroic lower oceanic crust from plagioclase lattice preferred orientation in the Samail ophiolite. *Earth and Planetary Science Letters*, *427*, 249–261. https://doi.org/10.1016/j.epsl.2015.07.001
Vanderbeek, B. P., & Toomey, D. R. (2017). Shallow mantle anisotropy beneath the Juan de Fuca plate. *Geophysical Research Letters*, *44*, 382–389. https://doi.org/10.1002/2017GL074769
Visser, K., Trampert, J., & Kennett, B. L. N. (2008). Global anisotropic phase velocity maps for higher mode Love and Rayleigh waves. *Geophysical Journal International*, *172*, 1016–1032. https://doi.org/10.1111/j.1365-246X.2007.03685.x
Warren, J. M., Hirth, G., & Kelemen, P. B. (2008). Evolution of olivine lattice preferred orientation during simple shear in the mantle. *Earth and Planetary Science Letters*, *272*, 501–512. https://doi.org/10.1016/j.epsl.2008.03.063
Webber, C., Newman, J., Holyoke, C. W. III., Little, T., & Tikoff, B. (2010). Fabric development in cm-scale shear zones in ultramafic rocks, Red Hills, New Zealand. *Tectonophysics*, *489*, 55–75. https://doi.org/10.1016/j.tecto.2010.04.001
Weeraratne, D. S., Forsyth, D. W., Yang, Y., & Webb, S. C. (2007). Rayleigh wave tomography beneath intraplate volcanic ridges in the South Pacific. *Journal of Geophysical Research*, *112*, B06303. https://doi.org/10.1029/2006JB004403
Yuan, K., & Beghein, C. (2013). Seismic anisotropy changes across upper mantle phase transitions. *Earth and Planetary Science Letters*, *374*, 132–144. https://doi.org/10.1016/j.epsl.2013.05.031
Yuan, K., & Beghein, C. (2014). Three-dimensional variations in Love and Rayleigh wave azimuthal anisotropy for the upper 800km of the mantle. *Journal of Geophysical Research: Solid Earth*, *119*, 3232–3255. https://doi.org/10.1002/2013JB010853
Zhang, S., & Karato, S. (1995). Lattice preferred orientation of olivine aggregates deformed in simple shear. *Nature*, *375*, 774–777.